Quaternary Science Reviews 203 (2019) 151–169

Contents lists available at ScienceDirect

Quaternary Science Reviews

journal homepage: www.elsevier.com/locate/quascirev

Late Holocene sea-level changes in eastern Québec and potential drivers

R.L. Barnett [a, b, *], P. Bernatchez [b], M. Garneau [c], M.J. Brain [d], D.J. Charman [a], D.B. Stephenson [e], S. Haley [a], N. Sanderson [a]

[a] Geography, College of Life and Environmental Sciences, University of Exeter, Amory Building, Rennes Drive, EX4 4RJ, UK
[b] Chaire de recherche en géoscience côtière, Université du Québec à Rimouski, Québec-Océan et Centre d'études nordiques, 300 Allée des Ursulines, Rimouski, Québec, G5L 3A1, Canada
[c] Chaire de recherche sur la Dynamique des Écosystèmes Tourbeux et Changements Climatiques, Université du Québec à Montréal, Centre GEOTOP, CP 8888, Succ. Centre-Ville, Montréal, Québec, H3C 3P8, Canada
[d] Department of Geography, Durham University, Lower Mountjoy, South Road, Durham, DH1 3LE, UK
[e] Mathematics, College of Engineering, Mathematics and Physical Sciences, University of Exeter, Harrison Building, North Park Road, EX4 4QF, UK

ARTICLE INFO

Article history:
Received 1 April 2018
Received in revised form
29 October 2018
Accepted 31 October 2018

Keywords:
Holocene
Sea level
North Atlantic
Quebec
Canada
Foraminifera
Salt marsh
Little ice age
Micropalaeontology

ABSTRACT

Late Holocene sea-level changes can be reconstructed from salt-marsh sediments with decimetre-scale precision and decadal-scale resolution. These records of relative sea-level changes comprise the net sea-level contributions from mechanisms that act across local, regional and global scales. Recent efforts help to constrain the relative significance of these mechanisms that include sediment dynamics and isostasy, which cause relative sea-level changes via vertical land motion, ocean-atmosphere processes that influence regional-scale ocean mass redistribution, and ocean-cryosphere and steric interactions that drive global scale ocean-volume changes. There remains a paucity of high-resolution Late Holocene sea-level data from eastern Canada. This precludes an interrogation of the mechanisms that define sea-level changes over recent centuries and millennia in a region sensitive to oceanic (Atlantic Multidecadal Variability, Atlantic Meridional Overturning Circulation), atmospheric (North Atlantic Oscillation, Arctic Oscillation) and cryospheric (ice-mass balance) changes. We present new relative sea-level data that span the past three millennia from Baie des Chaleurs in the Gulf of St. Lawrence generated using salt-marsh foraminifera supported with plant macrofossil analyses. The accompanying chronology is based on radiocarbon and radionuclide analyses, which are independently verified using trace metal and microcharcoal records. Relative sea level has risen at a mean rate of 0.93 ± 1.25 mm yr^{-1} over the past ~1500 years. Residual structure within the reconstruction ('internal variability') has contributed up to an additional 0.61 ± 0.46 mm yr^{-1} of short-lived RSL rise prior to 1800 CE. Following a sea-level low stand during the Little Ice Age, acceleration in relative sea-level rise is identified between 1800 and 1900 CE within the estimates of internal variability and from 1950 CE to present in both the secular and residual trends. Phases of relative sea-level changes in the Gulf of St. Lawrence are concomitant with periods of glacier mass loss following the Little Ice Age, phase periods of the North Atlantic Oscillation and the Atlantic Meridional Overturning Circulation and Northern Hemisphere warming. Quantifying the individual effects of these different mechanisms is important for understanding how ocean-atmosphere processes redistribute ocean-mass upon larger scale background ocean-volume changes.

1. Introduction

Holocene relative sea-level (RSL) changes throughout eastern Canada have been dominated by patterns of vertical land motion (Koozhare et al., 2008; Peltier et al., 2015) resulting from deglaciation of the Laurentide Ice Sheet (LIS) and the Appalachian Glacier Complex (AGC) (Stea, 2004; Stea et al., 2011; Rémillard et al., 2016).

* Corresponding author. Geography, College of Life and Environmental Sciences, University of Exeter, Amory Building, Rennes Drive, EX4 4RJ, UK.
E-mail address: r.barnett@exeter.ac.uk (R.L. Barnett).

https://doi.org/10.1016/j.quascirev.2018.10.039
0277-3791/

This has produced a gradient in Late Holocene (past 4250 yrs) RSL trends that relate to proximity to former ice-sheet margins (Fig. 1). Coastlines closer to the centre of the former ice mass, such as those along the St Lawrence Estuary, have experienced near continuous emergence for the past ~3000 years (Dionne, 1985, 1990; 1996, 1997; 2001, 2002; Dionne and Coll, 1995; Dionne and Occhietti, 1996; Bernatchez, 2003). Coastlines located further south and east in Canada and towards the North Atlantic have experienced Late Holocene submergence (Scott et al., 1981, 1984; Scott and Greenberg, 1983; Gehrels, 1999; Gehrels et al., 2004; Barnett et al., 2017a), due to high rates of land subsidence associated with the collapse of the LIS forebulge. With the gradual abatement in rates of vertical land motion through the Holocene (Dyke and Peltier, 2000; Mitovica et al., 2000) and improvements in sea-level reconstruction techniques from proxy choice, age-depth modelling and statistical methods (c.f., Shennan et al., 2015), we are now better able to investigate RSL mechanisms that drive lower-magnitude and shorter-term changes than those caused by glacio-isostatic adjustment (GIA). However, there remains a paucity of suitable high-resolution and precise records from eastern Canada that allow appropriate exploration of these mechanisms.

Sea-level signals from ice melt, thermal expansion and ocean-atmosphere circulation processes are low in comparison to the GIA signal in RSL records from eastern Canada. Contributions from land-based ice melt originate predominantly from the Antarctic Ice Sheet after the Mid Holocene (Ullman et al., 2016). However, the termination of polar contributions to Late Holocene sea levels remains imprecisely constrained (Lambeck et al., 2014; Woodroffe et al., 2015; Bradley et al., 2016). With potential evidence of sustained warming in West Antarctica between 2500 and 2000 yrs BP (Fegyveresi et al., 2016), it is plausible that a Late Holocene Antarctic ice-melt signal may exist in eastern Canada, especially due to the sensitivity of the region to Southern Hemisphere melt sources (Mitrovica et al., 2001, 2009). More recent signals may also exist due to a cold and ice-loaded Antarctica during the Little Ice Age (Bertler et al., 2011), which likely contributed to sea-level rise after 1730 CE following this cold phase (Grinstead et al., 2009).

Ocean temperatures in the northwest North Atlantic (e.g., de Vernal and Hillaire-Marcel, 2006) followed the global temperature trend of gradual cooling (Marcott et al., 2013) through the Late Holocene. As such, it is unlikely that thermal expansion contributed much to sea-level trends in eastern Canada until the 19th century when mean global sea-level rise rapidly accelerated in line with global temperature (Kopp et al., 2016). In contrast to these long-period mechanisms, ocean-atmosphere processes operate across relatively shorter time frames. Phases of ocean circulation (via the Atlantic Meridional Overturning Circulation; AMOC), sea-surface temperature distribution (via the Atlantic Multidecadal Oscillation; AMO) and atmospheric modes (via the North Atlantic Oscillation; NAO) are intercorrelated (McCarthy et al., 2015) and exhibit phase periods across annual (Cunningham et al., 2007), multi-decadal (Curry et al., 1998; Bryden et al., 2014; Trouet et al., 2009), centennial (Hall et al., 2004; Wanamaker et al., 2012) and millennial (McManus et al., 2004; Böhm et al., 2015) scales. These processes set up baroclinic gradients in the North Atlantic that drive spatially uneven patterns of RSL changes across a range of timescales (e.g., Sallenger et al., 2012; Ezer, 2013; Saher et al., 2015). Changes in North Atlantic circulation strength over the past

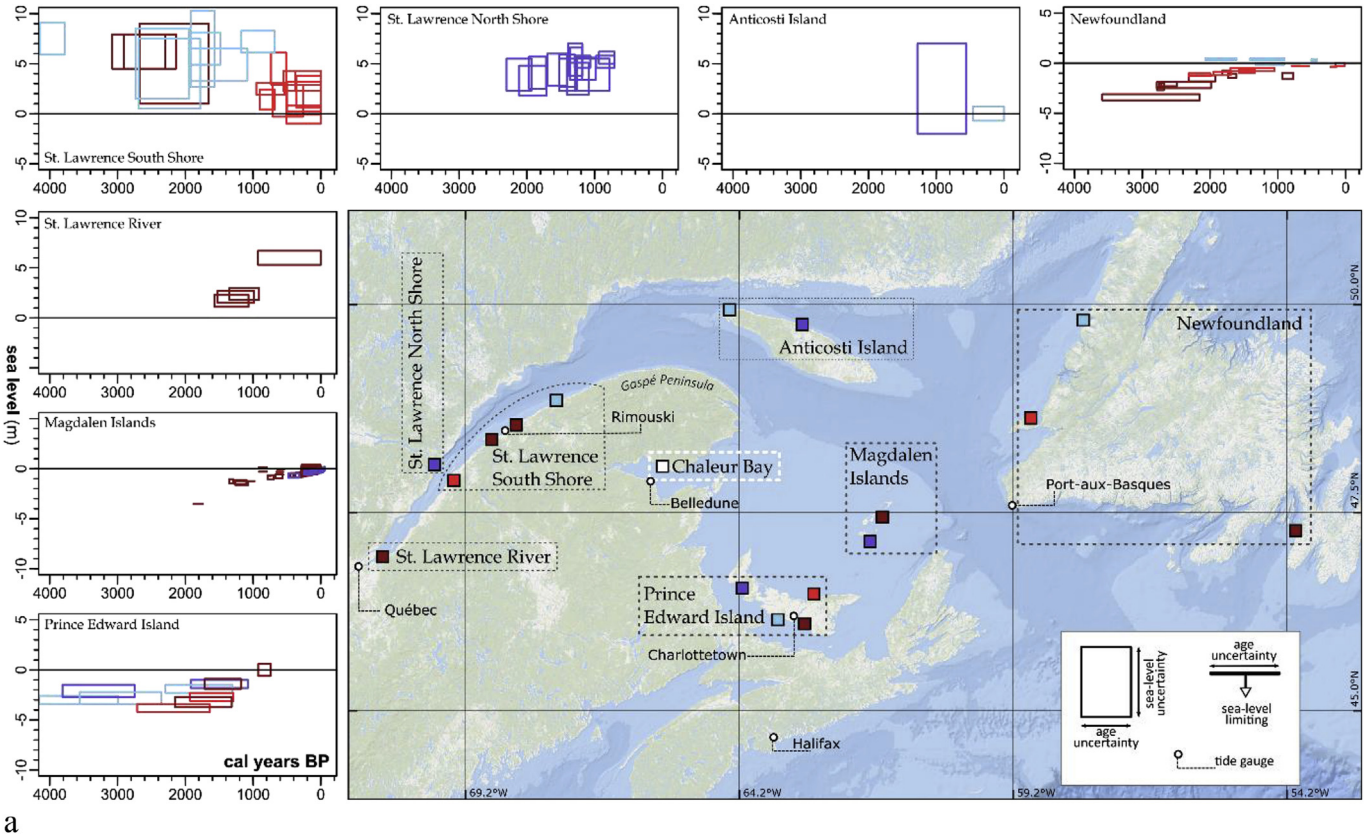

Fig. 1. Location map of eastern Canada and the Gulf of St. Lawrence. The study site in the Baie des Chaleurs (white square) with locations of primary tide-gauge stations (circles) and sources of Late Holocene RSL data (collated by Vacchi et al., 2018) from the St Lawrence Estuary (Dionne, 1990, 1996; 1997, 1999; 2001; Dionne and Coll, 1995; Dyke, 2004), Anticosti Island Dubois et al. (1985), Prince Edward Island (Frankel and Crowl, 1961; Scott et al., 1981), Magdalen Islands (Barnett et al., 2017a) and Newfoundland (Brookes et al., 1985; Wright and van de Plassche, 2001; Daly et al., 2007).

millennium (Rahmstorf et al., 2015) correlate with RSL variations observed along the eastern sea-board of North America (Gehrels, 1999; Gehrels et al., 2002; Kemp et al., 2011, 2013, 2014, 2015, 2017a). However, attributing multiscalar RSL trends to causal mechanisms remains a significant challenge due to the complexity of the signals related to the different drivers of change (e.g., Kemp et al., 2017b).

Distinguishing between processes that contribute to ocean volume expansion (e.g., polar ice-melt and thermal expansion) from those that redistribute ocean mass (e.g., AMOC) is necessary for developing accurate predictions of future regional sea-level changes. In regions experiencing higher-than global average RSL rise, such as locations within the Gulf of St. Lawrence (e.g., Han et al., 2014; Barnett et al., 2017a), phases of ocean-atmosphere processes may drive yet higher rates of local to regional RSL rise, further exacerbating the effects of land subsidence and global mean sea-level rise (Slangen et al., 2016). Therefore, the aim of this study is to develop new Late Holocene reconstructed RSL data for eastern Canada that are suitable for investigating the roles of different sea-level mechanisms across multidecadal to millennial timescales. We present a RSL reconstruction from eastern Québec with decimetre scale precision that is derived using salt-marsh foraminifera (Scott and Medioli, 1978; Edwards and Wright, 2015) and plant macrofossils. The record differs from existing east coast North American Late Holocene RSL reconstructions as the site is separate from the North Atlantic sea-board and will provide new insight into ocean-atmosphere processes that are hypothesised to drive (multi-) centennial scale, spatially variable RSL changes in the North Atlantic (e.g., Saher et al., 2015; Kemp et al., 2018).

2. Geographic setting

2.1. Regional physiography

The Gaspé Peninsula in eastern Québec protrudes into the Gulf of St. Lawrence and is confined by the St Lawrence Estuary to the north and the Baie des Chaleurs to the south (Fig. 1). The geology of the Gaspé Peninsula is dominated by the Humber and Dunnage zones of the Paleozoic Appalachain Orogeny (Williams, 1979). Carboniferous Windsor Group units characterise the Gaspé southern shoreline along the Baie des Chaleurs (Brisebois, 1981) and the Bonaventure Formation from this Group (Alcock, 1935) provides the geological setting of clastic sandstone bedrock for the fieldwork locations.

The Baie des Chaleurs was marine inundated by 12,600 ± 200 cal yrs BP (Olejczyk and Gray, 2007) following deglaciation and retreat of the Gaspesie (Olejczyk and Gray, 2007) and Escuminac ice caps (Pronk et al., 1989; Bail, 1985) and the eastern limit of the LIS. After reaching a postglacial marine limit of 45–55 m on the north shore of the Baie des Chaleurs (Veillette and Cloutier, 1993), RSL dropped below the present-day level around 12,000 cal yrs BP (Thomas et al., 1973). Rapid isostatic recovery created a RSL low stand of between −20 and −30 m during the early Holocene (Grant, 1975), after which a continual transgression trend occurred through to present day (Schafer, 1977; Syvitski, 1992). Tidal range amplitudes vary from 2 to 3 m throughout the bay (Syvitski, 1992) and contemporary wave climate sees ~2 m wave swell rising to ~5 m during stormy conditions (Schafer, 1977).

2.2. Study sites

The studied sites are located on the northern shore of the Baie des Chaleurs (Fig. 2a). One site (Fig. 2b) is located at Saint-Siméon near to Bonaventure and the second site is located at Saint-Omer, ~50 km to the west (Fig. 2c). Surface vegetation for the two sites is characteristic of intertidal salt marshes along the Gaspé Peninsula coastline (Tremblay, 2002) and throughout the Gulf of St. Lawrence (e.g., Dionne, 2004; Barnett et al., 2016). *Myrica gale* is prevalent at the transition between intertidal and supratidal environments. High-marsh flora includes widespread *Spartina patens* as well as *Juncus* spp., *Schoenoplectus* spp. and *Glaux maritima*. *Spartina alterniflora* and *Salicornia depressa* occupy low-marsh elevations and *Zostera marina* characterises low-intertidal and shallow subtidal environments. Collin et al. (2010) reported quantitative vegetation descriptions for the marsh at Saint-Siméon.

A tide gauge at Belledune, New Brunswick, is located 25 km to the southwest on the southern shoreline of the Baie des Chaleurs (Fig. 2a). Water-level data collected using Solinst Levelogger and Barologger data-loggers at Saint-Siméon during the fieldwork season showed excellent agreement ($r^2 = 0.99$) with tidal data recorded at Belledune (Fig. 3). As such, the tidal regime at the study sites is assumed to be broadly equivalent to that at Belledune. Mean tidal range (mean high water to mean low water) is 1.3 m and the difference between mean higher high water (MHHW) and mean lower low water (MLLW) during spring tides is 2.6 m (Fisheries and Oceans Canada Service; www.dfo-mpo.gc.ca). Tidal characteristics used in this study are shown in Fig. 3 relative to Chart Datum and have been converted to the Canadian Geodetic Vertical Datum of 1928 (CGVD28) using benchmark vertical offsets at Belledune (BM: 98B9000).

3. Methods

3.1. Field methods

Fieldwork was carried out in July 2016 at both sites. Surface profile transects (Fig. 2b and c) ran from tidal mud-flats up into the supratidal zones and were surveyed at each site using Differential Global Positioning System (Trimble R4 RTK base station, Trimble R10 rover; ±0.015 m vertical uncertainty) relative to the Canadian Spatial Reference System North American Datum 1983. Elevation was measured relative to CGVD28 following a correction from the geoid model HT2.0. Vertical offsets between Chart Datum and CGVD28 at nearby benchmarks in Carleton, Québec (BM: 10L1400) and Belledune, New Brunswick (BM: 98B9000) were used to convert elevation solutions between tidal and geodetic datums.

Samples of the marsh surface (top 1 cm) were collected along three transects at Saint-Siméon ($n = 68$) and Saint-Omer ($n = 55$) at 0.03–0.05 m vertical intervals. These were subsampled (2 cm^{-3}) for foraminifera and stained within two weeks of collection using Rose Bengal in a 30% C_2H_5OH: H_2O solution to differentiate between live (stained) and fossilised (unstained) foraminifera tests (Murray, 1976). The lithostratigraphy at Saint-Siméon was established from creek-scarp sections at low tide, which were cut back to reveal clean and undisturbed sediment sequences that appeared free from winter ice-related surface erosion. The facies were described following Long et al. (1999; after Troels-Smith, 1955). The depth to base was established using an Eijkelkamp narrow-gauge gouge auger. Fossil material for palaeoenvironmental analyses were collected from the creek-scarp sections in the field using monolith tins. Monoliths were used over alternative methods in order to minimise the potential of vertical mixing, compaction and shearing of the sediment during recovery and to provide larger volumes of sediment for analyses.

3.2. Training set and transfer function

Foraminifera preparations followed Gehrels (2002) after Scott and Medioli (1980). Taxonomy followed Murray (1971, 1979) and taxon groupings were established in accordance with regional

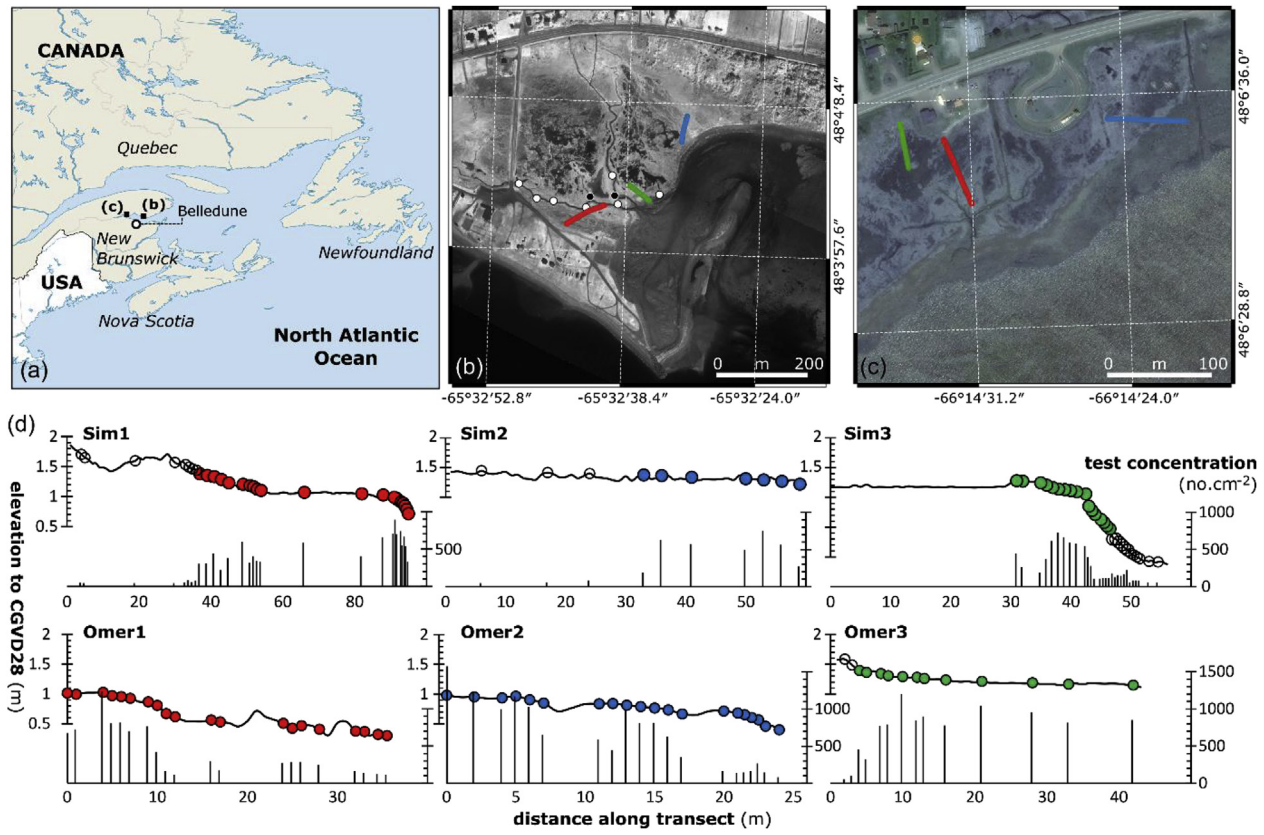

Fig. 2. Fieldwork location sites in the Baie des Chaleurs. (a) Location of field sites at Saint-Siméon (b) and Saint-Omer (c) and the Belledune tide-gauge station. (b) Location of surface transects (Sim1 - *red*; Sim2 - *blue*; Sim3 - *green*) and location of stratigraphy description sites (*circles*) and monoliths collected for palaeoenvironmental analyses (*filled circles*) at Saint-Siméon. (c) Location of surface transects (Omer1 - *red*; Omer2 - *blue*; Omer3 - *green*) at Saint-Omer. (d) Surface transect elevation profiles (*primary axes*) and concentration of foraminifera tests in surface samples (*secondary axes*) at Saint-Siméon (*top row*) and Saint-Omer (*bottom row*). Coloured circles denote samples used in the training set and empty circles denote samples that lack high concentrations of foraminifera. (For interpretation of the references to colour in this figure legend, the reader is referred to the Web version of this article.)

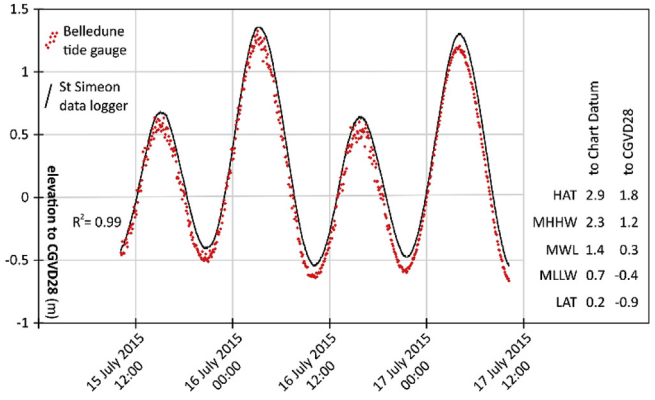

Fig. 3. Tidal characteristics. Water-level datalogger solutions from Saint-Siméon compared against contemporaneous tide-gauge water-level data from the station at Belledune, New Brunswick, located 25 km to the southwest. The tidal regime at Belledune (shown relative to Chart Datum and CGVD28) is taken to be broadly equal to that at the fieldwork sites.

datasets (Wright et al., 2011; Kemp et al., 2015). In summary, species of *Haplophragmoides* were combined into a single group, as were *Ammobaculites* spp., *Reophax* spp., *Textularia* spp. and calcareous forms. Counts of *Siphotrochammina lobata* were incorporated into those of *Trochammina inflata* and forms of *Balticammina pseudomacrescens* and *Jadammina macrescens* were differentiated on account of independent ecological ranges (Gehrels and van de Plassche, 1999). Counts were carried out on up to 2 cm^{-3} of sediment and sample mean count totals of unstained tests for Saint-Siméon and Saint Omer were $n = 324$ and $n = 294$ respectively.

A regional training set of salt-marsh surface foraminifera was built using data available from the Gulf of St. Lawrence (Fig. 4a). This approach increases the availability of modern analogues, expands the sampled environmental gradient and allows for more robust RSL reconstructions (e.g., Horton and Edwards, 2006). The training set comprised the 45 samples from Saint-Siméon and 52 samples from Saint-Omer (this study), 37 samples from Hynes Brook, Newfoundland (Wright et al., 2011) and 39 samples from the Magdalen Islands, Québec (Barnett et al., 2016). Due to the taxonomic separation of *B. pseudomacrescens* and *J. macrescens* (Gehrels and van de Plassche, 1999), earlier datasets from the region that combine these two taxa were omitted.

A standardised water level index (SWLI) was calculated for each surface sample based on its elevation above local mean water level (MWL) to normalise sample elevations between sites (c.f., Gehrels, 1999; Horton et al., 1999). The reference levels used to calculate SWLI were sample elevation above MWL; highest extent of foraminifera (HOF) as the upper reference level and MWL as the lower reference level (c.f., Wright et al., 2011).

The capability of the training set to predict marsh-surface elevations was assessed using a suite of regression model transfer functions in R (R Development Core Team, 2017) using rioja v0.9-9 (Juggins, 2015). Detrended canonical correspondence analysis was

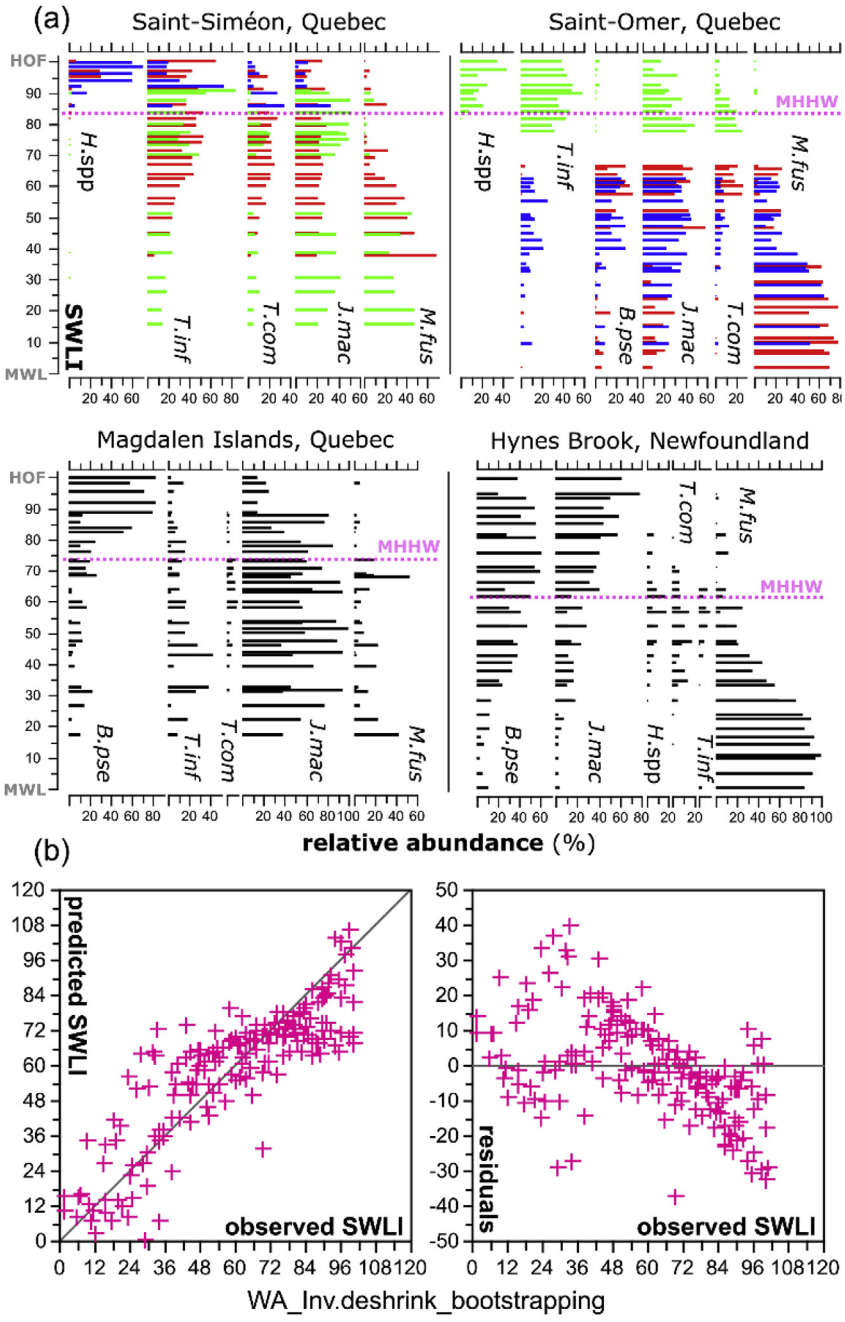

Fig. 4. Foraminifera training set data. (a) New surface foraminifera assemblages (showing dominant taxa only) developed in this study from Saint-Siméon and Saint-Omer in the Baie des Chaleurs plotted against a standardised water level index (SWLI) with highest extent of foraminifera (HOF) and mean water level (MWL) shown. Colours correspond to the surface transects displayed in Fig. 2. Also shown are published datasets from the Magdalen Islands (Barnett et al., 2016) and Newfoundland (Wright et al., 2011) used in the development of the training set applied in this study. (b) Transfer function observed versus predicted values and residuals using a weighted-averaging regression model with inverse deshrinking and bootstrapping cross-validation. Foraminifera abbreviations are as follows: *B.pse* = *Balticammina pseudomacrescens*; *H.*spp. = *Haplophragmoides* spp.; *J.mac* = *Jadammina macrescens*; *T.com* = *Trochammina comprimata*; *T.inf* = *Trochammina inflata*; *M.fus* = *Miliammina fusca*. (For interpretation of the references to colour in this figure legend, the reader is referred to the Web version of this article.)

first applied to determine assemblage compositional turnover along the gradient of elevation (ter Braak and Prentice, 1988) using Canoco 5 (ter Braak and Šmilauer, 2012). Training set turnover was calculated at 3.5 standard deviation units (axis 1 eigenvalue = 0.49) and weighted averaging (WA; ter Braak and Looman, 1986) regression models with both inverse and classical deshrinking methods (Birks et al., 1990) were chosen as they are suitable for datasets displaying unimodal species response to changing elevation (Birks, 1995). Bootstrapping (Stine, 1990) and leave-one-site-out (Manly, 1997) cross-validation techniques were both used to analyse transfer function performance and check for spatial autocorrelation within the training set (Telford and Birks, 2005).

3.3. Sediment analyses

Retrieved sediments were analysed for foraminifera using the preparation procedures outlined above (Gehrels, 1999). The monolith selected for RSL reconstruction (SimVII; Fig. 5) was

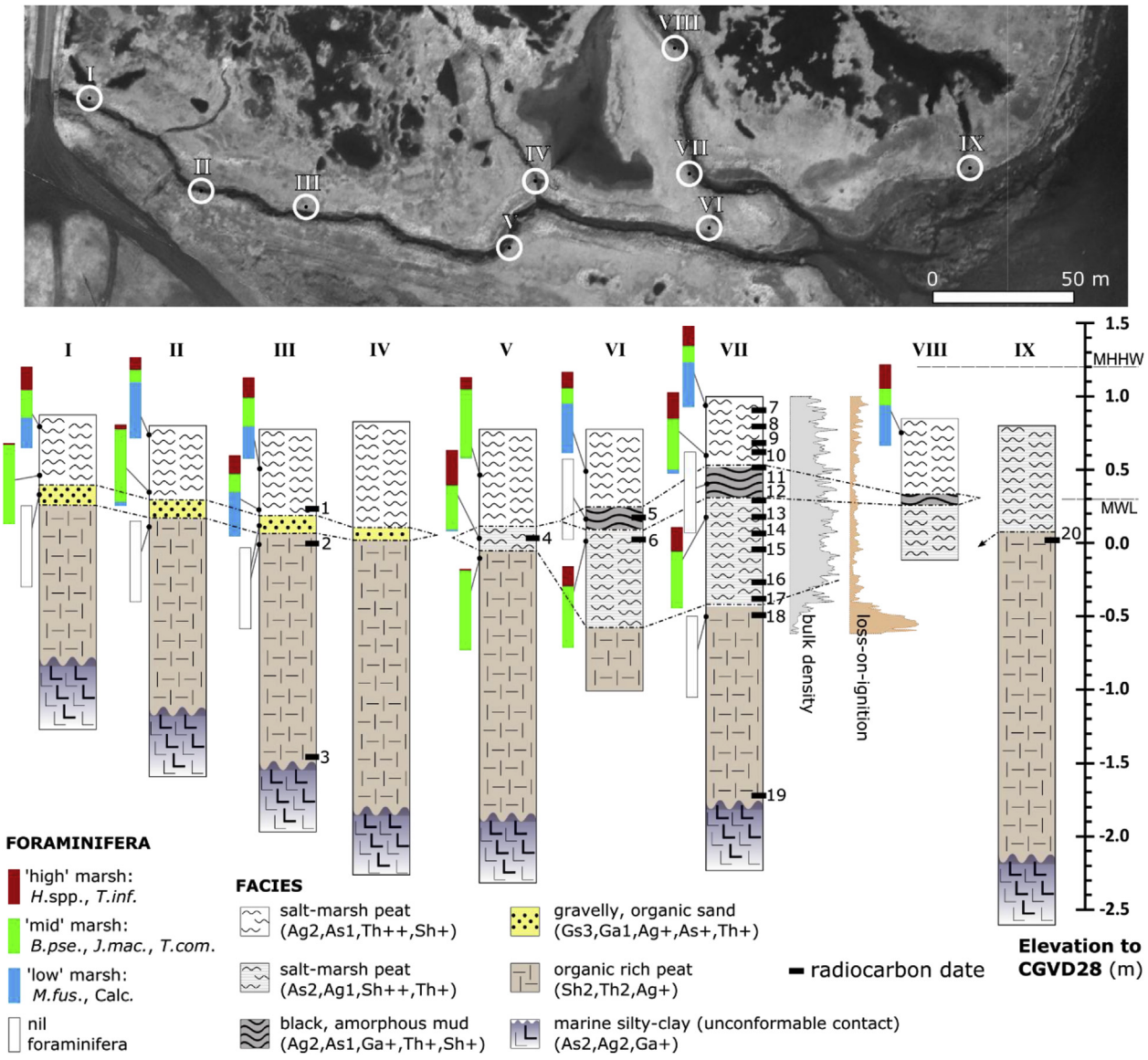

Fig. 5. Lithostratigraphy at Saint-Siméon. Location of sediment-description sites at Saint-Siméon with described subsurface lithology following Long et al. (1999) and relative abundance of foraminifera that have been grouped into low-, mid- and high-marsh taxa. (*B.pse* = *Balticammina pseudomacrescens*; Calc. = calcareous forms; *H.*spp. = *Haplophragmoides* spp.; *J.mac* = *Jadammina macrescens*; *T.com* = *Trochammina comprimata*; *T.inf* = *Trochammina inflata*; *M.fus* = *Miliammina fusca*). Monolith VII underwent high-resolution palaeoenvironmental analyses and the top 0.23 m of monolith IV was used to generate a second sea-level reconstruction to help validate the primary reconstruction from monolith VIII. Bulk density and LOI values are shown for monolith SimVII.

subsampled at 1 cm resolution from 0 to 135 cm, below which foraminifera were absent. The top 30 cm of a second monolith (SimIV; Fig. 5) was subsampled for foraminifera at 0.5 cm resolution to develop a second reconstruction of RSL changes for the past ~200 years. This reconstruction was used to validate RSL trends, timings and magnitudes from monolith SimVII and to test the influence that sampling resolution had on reconstruction results.

The reconstruction monolith SimVII was also sampled for wider palaeoenvironmental analyses. Plant macrofossil sampling (Barber et al., 1994; Garneau, 1998; Mauquoy and van Geel, 2007) was carried out at 5 cm resolution, which supported qualitative palaeoenvironmental descriptions and provided material for radiocarbon dating. Loss-on-ignition (Ball, 1964; Plater et al., 2015) was measured at 1 cm depth intervals to provide estimates of organic and mineral contents through the monolith to support palaeoenvironmental interpretations. Microcharcoals were analysed following Whitlock and Larsen (2001) and used as an indicator of local fire regime (Clark and Royall, 1996), providing a qualitative tool to help validate the independent chronology of monolith SimVII. Dry bulk density was also measured at 1 cm depth intervals down to 150 cm to assist in descriptions and interpretations of lithofacies.

3.4. Chronology and age-depth modelling

Material for conventional AMS radiocarbon dating (Stuiver and Polach, 1977) was picked from the plant macrofossil preparations (c.f., Garneau, 1998) following identification (Table 1). Samples were sent to the Laboratoire de Radiochronologie at the Centre d'études nordiques, Université Laval, for pretreatment and $\delta^{13}C$ analysis, and to the Keck Carbon Cycle AMS Laboratory, University of California, for ^{14}C dating. Radiocarbon ages were calibrated in CALIB v7.10 (Stuiver and Reimer, 1986) using the IntCal09 calibration curve (Reimer et al., 2009) to provide calendar dates.

Table 1
Radiocarbon samples and results for cores SimIII, V, VI, VII, and IX at Saint-Siméon. Sample numbers correspond with the locations shown in Fig. 5.

#	Lab code (ULA)	Core (depth, m)	Material	Δ ^{14}C (‰)	^{14}C a BP (±2 σ)	Δ ^{13}C (‰)
1	6018	III (0.55)	Herbaceae stems	−27 ± 2.7	220 ± 25	−26.9
2	6019	III (0.75)	Herbaceae stems & rhizomes	−150.5 ± 1.7	1310 ± 20	−19.2
3	6008	III (2.22)	Ericaceae bud	−232.4 ± 1.9	2125 ± 20	−25.9
4	6021	V (0.75)	Herbaceae stems & rhizomes	−137.0 ± 2.1	1185 ± 20	−26.4
5	6022	VI (0.60)	Seeds (*Schoenoplectus, Eleocharis*) & Ericaceae leaves	−87.2 ± 1.9	735 ± 20	−26.2
6	6023	VI (0.76)	Herbaceae rhizomes	−124.7 ± 1.7	1070 ± 20	−14.5
7	6295	VII (0.10)	Herbaceae stems & rhizomes	235.9 ± 2.5	–	−16.3
8	6296	VII (0.20)	Herbaceae stems & rhizomes	2.2 ± 2.0	–	−14.5
9	6297	VII (0.30)	Seeds (*Suaeda*)	−20.6 ± 2.0	165 ± 20	−28.1
10	6298	VII (0.36)	Herbaceae stems & rhizomes	−28.0 ± 1.9	230 ± 20	−14.8
11	6299	VII (0.45)	Herbaceae stems & rhizomes	−94.7 ± 2.1	800 ± 20	−22.1
12	6300	VII (0.66)	Herbaceae stems & rhizomes, Ericaceae spindles	−69.2 ± 1.8	575 ± 20	−23.1
13	6301	VII (0.80)	Herbaceae stems & rhizomes	−79.1 ± 1.8	660 ± 20	−13.9
14	6302	VII (0.90)	Herbaceae stems & rhizomes	−123.4 ± 1.7	1060 ± 20	−13.1
15	6303	VII (1.00)	Herbaceae stems & rhizomes	−135.3 ± 2.0	1170 ± 20	−13.5
16	6304	VII (1.20)	Herbaceae stems & rhizomes	−139.9 ± 1.9	1210 ± 20	−14.2
17	6024	VII (1.30)	Seeds (*Schoenoplectus*) & Lignose branchlets	−176.3 ± 1.7	1560 ± 20	−26.5
18	6025	VII (1.40)	Seeds (*Schoenoplectus & Scirpus*) & Ericaceae spindles	−217.5 ± 1.7	1970 ± 20	−25.7
19	6020	VII (2.67)	Coniferae needles & Ericaceae bark	−301.8 ± 1.9	2885 ± 25	−27.9
20	6009	IX (0.82)	Lignose branch	−240.4 ± 1.5	2210 ± 20	−23.2

The reconstruction (SimVII) and validation (SimIV) monoliths were sampled for ^{210}Pb radionuclide analysis down to 27 cm depth and at equivalent resolutions to foraminiferal analyses. Sample ^{210}Pb activity was determined by measuring alpha decay of its daughter product ^{210}Po as a proxy (Flynn, 1968; El-Daoushy et al., 1991). A subsample of freeze-dried and homogenised sediment was spiked with a ^{209}Po chemical yield tracer, acid digested using sequential HNO_3:H_2O_2:HCl (1:2:1) chemical washes at 90 °C, and then extracted from the solution, electroplated onto a silver disc, and measured using the Ortec Alpha Ensemble Integrated Alpha-Spectrometry Suite at the University of Exeter, Geography Radiometry Laboratory, United Kingdom. The constant rate of supply model (CRS) was applied to calculate age-depth profiles based on total ^{210}Pb inventory, sample-specific activity and cumulative mass (Appleby, 2001). The equilibrium depth, the point at which excess ^{210}Pb activity decays to the equivalent activity of supported ^{210}Pb (c.f., Corbett and Walsh, 2015), was defined as the depth where sample activity was less than the mean activity of the samples below. Activity profiles for the lower most samples from both monoliths were modelled using a power function (Campbell, 1996) to remove the effects of bulk density variability on activity and aid in the determination of the equilibrium depth.

Radiocarbon and ^{210}Pb ages from the SimVII monolith were used to develop an age-depth model using Bacon v2.2 (Blaauw and Christen, 2011) within R (R Development Core Team, 2017) following standard practices (e.g., Barlow et al., 2014; Saher et al., 2015; Barnett et al., 2017a). Radiocarbon age results were calibrated within Bacon using the IntCal09 (Reimer et al., 2009) or the post-bomb NH1 (Hua and Barbetti, 2004) calibration curves as appropriate. Input ages were modelled using Student-t test distributions with wide tails to permit the inclusion of potential outliers (Christen and Pérez, 2009; Blaauw and Christen, 2011). Bayesian priors for the accumulation rate variability within the model (*mem.mean = 0.4* and *mem.strength = 3*) were set to reflect the evolution in lithostratigraphic sub-facies. Age-depth profile means and 2σ uncertainties at 0.01 m contiguous intervals were derived from Markov Chain Monte Carlo (MCMC) iterations.

The ^{210}Pb age-depth profiles and age modelling in Bacon were validated using geochemical profiles of trace metals (Cd, Cr, Cu, Ni, Pb, Zn), which provided independent pollutant chronomarkers (Marshall, 2015). Sediment subsamples were prepared following Environmental Agency (2006) guidelines: air-dried sample was added to a 1:3 HNO_3:HCl digest, filtered and prepared for solution in deionised H_2O. Machine runs with replicate sampling were undertaken on a Varian Vista-MPX inductively coupled plasma optical emission spectrometer at the University of Exeter with sequential blanks and standards (Merck Millipore ICP multi-element standard solution IV). Element concentrations (mg l^{-1}) were normalised against the lithophile Fe to create enrichment factor profiles following Klaminder et al. (2003). Enrichment factor trends in Pb that correlated with continent-wide signals driven by leaded-gasoline consumption and regulation (Nriagu, 1990; Graney et al., 1995; Blais, 1996) and trace heavy-metal pollutant trends that correlated with local industrial activity (Hildebrand, 1984; Parsons and Cranston, 2005, 2006; Fraser et al., 2011) were compared against the age-depth modelling results for Saint-Siméon.

3.5. Reconstructing RSL and estimation of errors

A weighted-averaging regression model applying inverse deshrinking was used to predict palaeo-marsh surface elevations (PMSEs) from fossil foraminifera assemblages in C2 (Juggins, 2003). Bootstrapping cross-validation ($n = 1000$) was used to provide root-mean-square-prediction-errors (RMSEP) for the PMSE of each sample. Fossil assemblages that lacked a modern analogue were removed from the reconstruction (Barlow et al., 2013). A squared chord dissimilarity measure (minDC) was applied to fossil assemblages using the modern analogue technique (MAT) in C2. Fossil assemblages with minDC values greater than the 20th percentile of modern assemblage distributions were removed from the reconstruction (Simpson, 2007; Watcham et al., 2013). Former RSL positions were calculated by subtracting PMSEs from sample elevations relative to the tidal frame (Gehrels, 1999). Each PMSE and RSL calculation was provided with a 2σ chronological constraint from the age-depth model.

3.5.1. Sediment compaction

Salt-marsh sediments are prone to compaction processes that can cause post-depositional lowering (PDL) of samples used to reconstruct RSL (Long et al., 2006; Brain, 2016). Compaction-induced PDL results in an overestimation of the magnitude and rate of reconstructed RSL rise (Horton and Shennan, 2009). It is therefore necessary to 'decompact' stratigraphic sequences to return core samples to their depositional elevations and avoid misinterpretations of the causes of RSL changes (Paul and Barras, 1998; Brain, 2015). We employed the geotechnical modelling framework

developed by Brain et al. (2011, 2015) to provide estimates of PDL downcore. This approach uses empirical, statistically-significant relationships between organic content (LOI) and the compression properties of contemporary salt-marsh sediments (Brain et al., 2012, 2015). By estimating LOI downcore, it is possible to assign compression properties to each layer in the core and, subsequently, run decompaction algorithms to provide depth-specific estimates of PDL, which is the height correction that is added to the *in situ* elevation of each sample used to reconstruct RSL. We employed a Monte-Carlo framework (5000 model runs) and specified uncertainties in input parameters to determine errors in each of these model outputs.

In the absence of local measurements of compression properties, we used the relationships between LOI and compression properties reported by Brain et al. (2017) for East River Marsh, Connecticut, United States, on the basis of relative geographic proximity (c.f., Brain et al., 2012, 2015) and the similar range of LOI values in the contemporary salt-marsh environment to those observed at Saint-Siméon. We used measured values of LOI in monolith SimVII to assign compression properties at 1 cm depth intervals at monolith depths between 0 and 135 cm that formed in intertidal environments. We applied a uniform error distribution (±1 percentage point) to account for LOI measurement uncertainty, randomly selecting values from the resulting distribution in each model run. For the underlying freshwater peat (135–270 cm), in each model run we randomly assigned values from a uniform probability distribution of LOI based on the mean (59.2%) and range (41.8%) of values observed in the upper 14 cm of the freshwater peat, for which LOI measurements were obtained (Fig. 5). We assigned values of specific gravity, G_s, to each 1 cm thick layer in the monolith using the predictive relationship provided by Hobbs (1986).

In contrast to relationships between LOI and compressibility, which ostensibly display inter-site comparability (Brain et al., 2015), one geotechnical property, namely yield stress (σ'_y), is controlled by local site conditions and so must be measured or estimated on a site-by-site basis. Accurately constraining values of σ'_y is important for modelling of compaction and PDL because it determines whether sediments exist in a low- or high-compressibility condition. Without local direct measurements, we determined values of σ'_y in the intertidal section of the monolith by calibration. We varied σ'_y in model runs until the model-generated downcore dry density profile most closely matched with monolith analysis (i.e., highest r^2_{adj} value, smallest standard errors and lowest p value between observed and model-predicted dry density values). To this end, we used a uniform probability distribution of σ'_y between 0.25 and 1.25 kPa. For the freshwater peat, we specified a uniform probability distribution between 15 and 25 kPa based on typical values (Long and Boylan, 2013). Following assignment of geotechnical properties to each 1 cm layer within the monolith, we used the Brain et al. (2011, 2012) model to obtain depth-specific estimates of dry density, effective stress, and PDL.

3.5.2. Estimating errors

Final reconstruction errors for each data point were calculated as the root-mean-square-errors of all resolved (2σ) uncertainties including surveying, sampling, regression modelling and decompaction errors (Preuss, 1979; Barlow et al., 2013). The primary sea-level reconstruction from monolith SimVII was validated using conventional techniques (Barlow et al., 2013; Kemp and Telford, 2015). First, the transfer-function based sea-level reconstruction for the SimVII top sample was compared against the surveyed core-top elevation as a check for reconstruction accuracy. The SimIV monolith was used to develop a comparable reconstruction for the past ~200 years to help validate the recent reconstruction from SimVII. Finally, the two transfer-function based reconstructions were compared against tide-gauge data from Belledune, New Brunswick, which is available for the past ~16 years. Tide-gauge water-level data was obtained from the Canadian Tides and Water Levels Data Archives (Fisheries and Oceans Canada) and smoothed to monthly means to allow more direct comparison with the resolution of the RSL reconstructions.

3.5.3. Estimating trends and internal variability

There are a variety of methods available for estimating trends from RSL data with constrained uncertainty (e.g., Cahill et al., 2015; Kopp et al., 2016). Here we treat the reconstruction as independent rather than use a spatio-temporal model in order to determine site specific rates of change. Unlike previous studies, we regress sea level estimates [$\boldsymbol{y_i}$] onto depth [$\boldsymbol{x_i}$] using generalised additive models (Hastie and Tibshirani, 1986, 1990; Wood, 2017) in the mgcv (Wood, 2018) R (R Development Core Team, 2017) package. By regressing onto depth rather than age, the method avoids assumptions of Gaussian probability distributions for x-axis uncertainties. An initial spline based smooth non-parametric link function [g] is used to estimate the long term background (secular) trend [$\boldsymbol{y_i} = g(\boldsymbol{x_i}) + \boldsymbol{z_i}$] plus residual variation [$\boldsymbol{z_i}$]. This estimate of secular trend allows us to explore residual variation (i.e., low amplitude variability and noise) whilst avoiding assumptions about local GIA rates from models that show discrepancies with observational data (e.g., Barnett et al., 2017a). Uncertainty in the secular trend was estimated by posteriorly mapping the trend from depth onto age [$g(\boldsymbol{x}) = g(\boldsymbol{f}(\boldsymbol{t}))$] using $n = 5000$ random MCMC simulations of age-depth profiles from Bacon (section 3.4) to provide probability distributions. The secular trend is a non-linear, slowly varying component that is taken to represent near-linear (i.e., GIA) and low-frequency geophysical processes. The residual variations are taken to represent auto-correlated high(er)-frequency variation [$\boldsymbol{z_i} = \boldsymbol{h}(\boldsymbol{x_i}) + \varepsilon_i$] plus independent noise [ε_i] (e.g., ecological noise and reconstruction error). This second spline-based regression is used to estimate 'internal variability' from the residual variation and uncertainty is estimated using MCMC age-depth profile outputs from Bacon as above.

4. Results

4.1. Modern foraminifera and the transfer function

Contemporary foraminifera samples from Saint-Siméon and Saint-Omer provided a total of 13 taxa or taxa groups (Supplementary Material). Foraminifera counts were sparse (<50 tests cm^{-3}) above 1.38 m CGVD28 at Saint-Siméon and above 1.39 m CGVD28 at Saint-Omer, marking the elevations of HOF at each site. Both sites displayed foraminifera distributions commonly seen on North Atlantic salt-marshes (e.g., Scott and Medioli, 1980; Gehrels and van de Plassche, 1999; Horton et al., 1999; Barnett et al., 2015) and further afield (e.g., Southall et al., 2006; Callard et al., 2011; Strachan et al., 2015, 2017). *Haplophragmoides* spp. was only common above MHHW where *T. inflata* was also present in high abundance (Fig. 4a). *J. macrescens* was found throughout the marshes and *T. comprimata* was most abundant near the level of MHHW. The abundance of *M. fusca* increased with decreasing elevation and typically dominated the lowest elevations of the marshes (Fig. 4a). Unvegetated mud flats occupied elevations below 0.47 m CGVD28 at Saint-Siméon, marking the lower boundary of the new training set at this location. Salt-marsh assemblages at Saint-Omer extended down to 0.30 m CGVD28, at mean water level (MWL) (Fig. 4a).

Modern foraminifera from Hynes Brook (Wright et al., 2011) and the Magdalen Islands (Barnett et al., 2016) used to develop the

transfer function show broadly comparable distributions to those that occur in the Baie des Chaleurs (Fig. 4a). There were some inconsistencies between sites, which demonstrates the value of using multiple sites to develop a training set that accurately replicates full regional ecological diversity. For example, *B. pseudomacrescens* is most abundant in the high marsh in the Magdalen Islands and in the high and mid-marsh at Hynes Brook. In contrast, this taxon is only dominant in the mid-marsh at Saint-Omer and is sparse throughout Saint-Siméon. The low-marsh species *M. fusca* dominates the assemblages below MHHW levels at all the sites except the Magdalen Islands where it is infrequently present. Barnett et al. (2016) assigned this to a lack of established low-marsh environments driven by rapid lateral erosion of the salt-marsh sediments.

Consistency in transfer function performance statistics when using bootstrapping and leave-one-site-out cross-validation suggests a lack of auto-correlation in the training set (Supplementary Material). The weighted-averaging regression model with inverse deshrinking used to predict PMSE values displays good correlation between observed and predicted sample elevations ($r^2 = 0.72$) and has a mean standard error of ±14.36 SWLI units (Fig. 4b). The equivalent 2σ site-specific transfer function error for Saint-Siméon is ±0.30 m. Transfer function residuals suggest that the model might under-predict sample elevations at the higher end of the gradient, which is often an artefact associated with inverse deshrinking methods. However, the reconstructions in this study predict PMSEs closer to the centre of the sampled gradient (i.e., between 40 and 80 SWLI) where model performance is most reliable (Fig. 4b).

4.2. Marsh lithostratigraphy and chronology

A basement of incompressible blue-grey silt-rich clay is found 1–3 m beneath the surface at Saint-Siméon following a NW-SE gradient in direction of the sea (Fig. 5). An organic and lignose rich peat with low dry bulk density is found above this basal clay, overlying an unconformable contact. Paired radiocarbon ages from the upper and lower contacts of this peat date inception of the unit from 2885 ± 25 and 2125 ± 20 ^{14}C a BP and transgression of the unit from 1970 ± 20 and 1310 ± 20 ^{14}C a BP (Table 1). The deposit was earliest established closest to the boundary of marine influence, persisted for approximately 1000 years, and was subsequently transgressed from the direction of the bay and overlain by the littoral deposits above (Fig. 5). Salt-marsh silts and clays are found above the peat deposit from 1560 ± 20 ^{14}C a BP onwards. Additional radiocarbon ages from the salt-marsh base (1185 ± 20 and 220 ± 25 ^{14}C a BP) demonstrate subsequent and continued transgression inland. Foraminifera typically found in the higher sections of salt marshes (e.g., *Haplophragmoides* spp., *T. inflata, J. macrescens, T. comprimata*) are common across the base of these sediments (Fig. 5). With continued accumulation, foraminifera associated with lower elevations (e.g., *M. fusca* and calcareous forms) become increasingly abundant. A black amorphous organic layer containing few foraminifera occurs within the salt-marsh deposits towards the east of the site, closer to the boundary of marine influence. The unit is found across much of the site and is dated to occur after 1070 ± 20 ^{14}C a BP. A sequence of radiocarbon ages from monolith SimVII document a reversal (Fig. 5, Table 1), suggesting that this unit may contain reworked material. Towards the west and the landward extent of the marsh, a gravelly-sand overlap deposit that thickens away from marine influence is found between the subsurface peat and the capping salt-marsh units. Radiocarbon ages constrain this unit to between 1310 ± 20 and 220 ± 25 ^{14}C a BP, indicating slow accumulation and subsequent transgression in the past few hundred years.

High-resolution sampling and analysis of monolith SimVII reveals the high organic content (>60% LOI) of the subsurface peat deposit below 140 cm depth. Foraminifera are sparse (<50 tests cm^{-3}) or absent at this point and deeper. Concentrations of foraminifera exceed 100 tests cm^{-3} above 135 cm depth, coinciding with increased bulk density and increased lithic content (Fig. 6). Typically high-marsh foraminifera (*Haplophragmoides* spp., *T. inflata, J. macrescens, B. pseudomacrescens*) are common between 135 and 70 cm. These assemblages coincide with evidence of sedges and cattails (*Schoenoplectus* spp., *Scirpus* spp., *Typha* spp.), common across eastern Canadian coastal marshes. The concentration of foraminifera and evidence of marshland flora declines between 70 and 36 cm depth. This coincides with the occasional presence of calcareous foraminifera in very low abundance (Fig. 6). Salt-marsh deposits return above 36 cm depth (characterised by *J. macrescens* and *T. inflata*), but also contain the low-marsh taxon *M. fusca*, with little evidence of the high-marsh taxa *Haplophragmoides* spp. and *B. pseudomacrescens*. These assemblages coincide with evidence of halophytic marsh flora such as seablite (*Suaeda maritima*) and glasswort (*Salicornia depressa*), which are common across frequently inundated elevations. The relative abundance of foraminifera in the top sediments of SimVII are replicated in the foraminifera analysis on core SimIV. The higher resolution analysis of SimIV provides additional detail to similar foraminifera trends that are seen in the top sediments of SimVII (Fig. 6b).

Analyses of the calcareous tests from the black amorphous layer in SimVII (36–70 cm) revealed substantial evidence of abrasion (c.f., Kotler et al., 1992) across the surface of the tests. This layer has an organic and lithic content that is consistent with the salt-marsh facies throughout the monolith (Fig. 6), yet is rich in fine grained (clay rich) sediment and also contains abundant bivalve shells and shell fragments, indicative of a low energy coastal aqueous environment. Additional microfaunal analysis revealed an absence of any established testate amoebae (c.f., Barnett et al., 2017b) populations throughout the layer. Combined with the very low abundance of foraminifera, it is likely that this layer does not represent a salt marsh or low-intertidal environment that was sampled in the modern surveys.

4.3. Reconstruction chronologies and age-depth modelling

A sequence of 13 radiocarbon ages supports the chronology for monolith SimVII. The subsurface peat unit is present between 2885 ± 25 and 1970 ± 25 ^{14}C a BP (Table 1), above which intertidal deposits occur to present-day. The two highest ^{14}C dates, from 10 to 20 cm depth, returned post-bomb (post-1950s) ages. Here, the ^{210}Pb analyses provide chronologies for the upper sediments of monoliths SimVII and SimIV (Fig. 7). The activity equilibrium depths were reached at 24 cm in both monoliths, above which the age-depth profiles corresponds to the past ~150 years (Fig. 7). The two profiles show comparable sedimentation rates (between ~1 and ~2 kg m^{-2} yr^{-1}) from ~1850 CE to ~2000 CE, at which point accumulation accelerates through to present-day. Slight discrepancies exist (up to 30 years) between the two age-depth profiles during the early 1900s and at this point the ^{210}Pb-derived ages display an offset with the post-bomb radiocarbon date from 20 cm depth, which was calibrated to 1954 to 1956 CE (Fig. 7).

Trace-metal enrichment profiles from SimVII provide validation for the ^{210}Pb-derived ages at several depths (Fig. 7). Onset of heavy-metal enrichment at 17 cm, corresponding to 1915 ± 4 CE (^{210}Pb age) can be attributed to pulp and paper-mill industries that became established in the Baie des Chaleurs from 1915 CE and continued for several decades (Hildebrand, 1984; Fraser et al., 2011). Secondary peaks in the same profiles at 11 cm (1967 ± 3 CE, ^{210}Pb age) can be attributed to industrial smelter activity that began in 1966 CE at Belledune, New Brunswick, (Hildebrand, 1984)

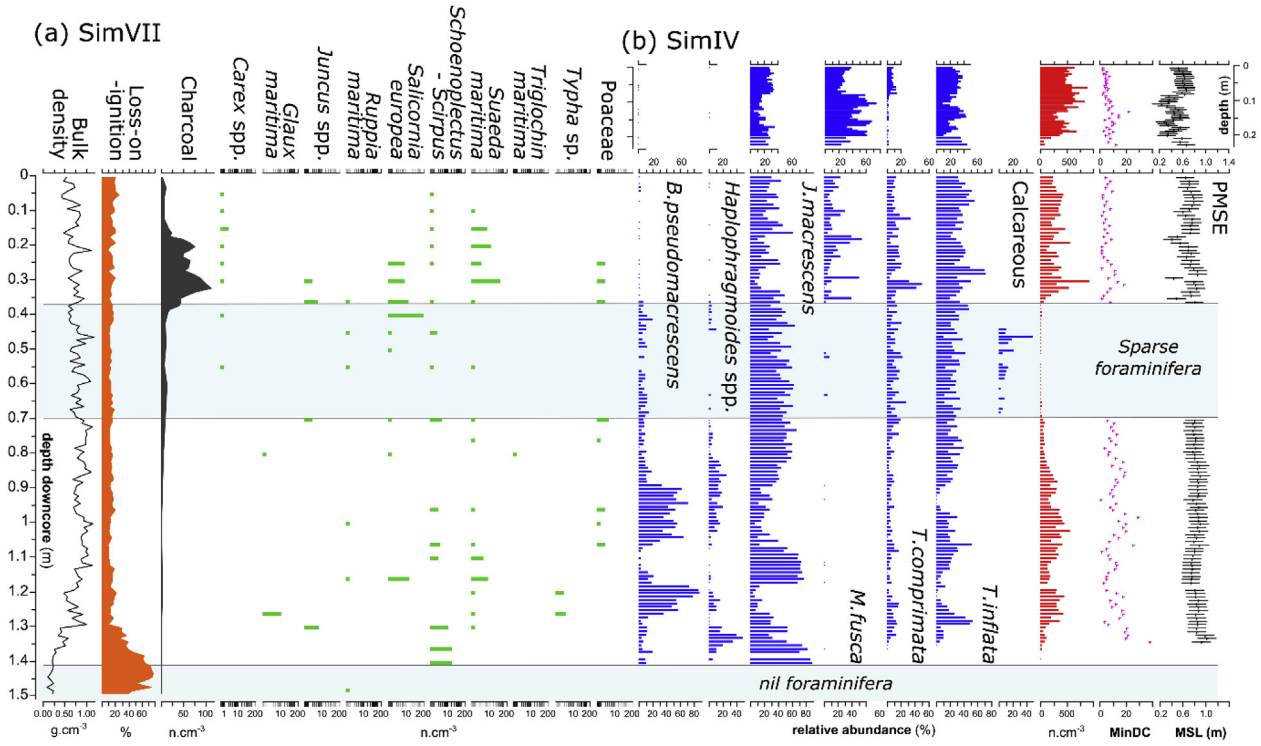

Fig. 6. Palaeoenvironmental analyses. Foraminifera assemblages (*blue*) are shown as relative abundance for monoliths SimVII (a) and SimIV (b) with corresponding sample test concentrations (*red*), modern analogue determinations (*MinDC*) and palaeo-surface elevation predictions (*PMSE*). Also shown are plant macrofossil concentrations (*green*), a microcharcoal record (*grey*) and lithological properties (bulk density and LOI) for monolith SimVII. (For interpretation of the references to colour in this figure legend, the reader is referred to the Web version of this article.)

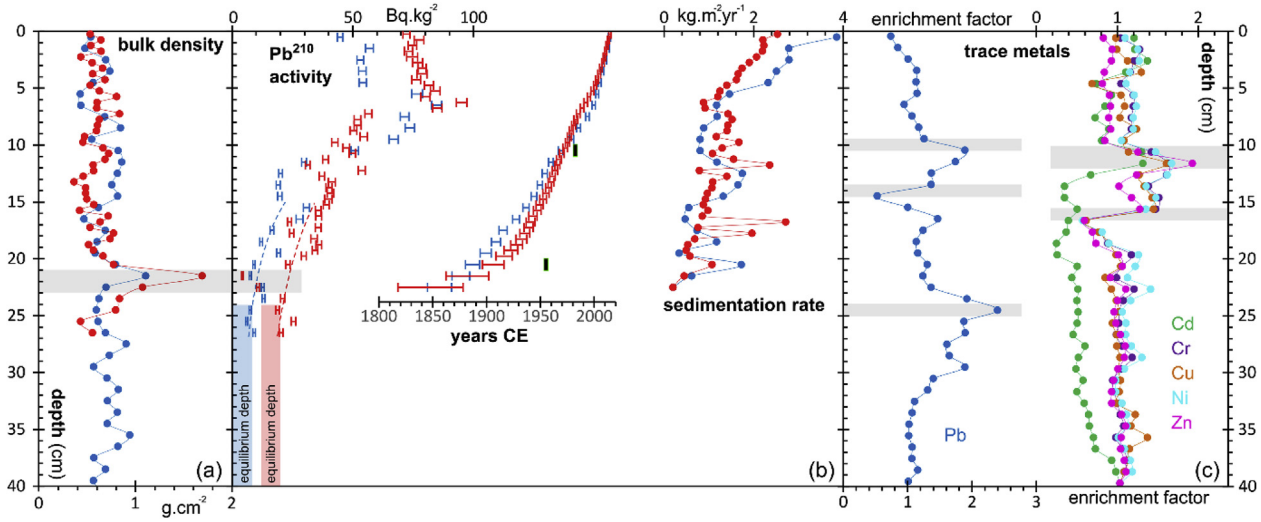

Fig. 7. Geochemical profiles. (a) Dry bulk density measurements of monoliths SimVII (*blue*) and SimIV (*red*) with influx of coarse grained sediment highlighted (*light grey*). (b) Radionuclide (^{210}Pb) activity and modelled age-depth profiles following Appleby (2001) with calibrated post-bomb radiocarbon ages (*black rectangles*) and modelled sedimentation rates for monoliths SimVII (*blue*) and SimIV (*red*). (c) Trace metal markers for monolith SimVII calculated as enrichment factors (see text for details) with features highlighted as chronohorizons for comparison with the age-depth model for monolith SimVII (*light grey*). (For interpretation of the references to colour in this figure legend, the reader is referred to the Web version of this article.)

and caused the distribution of pollutants throughout the bay (Parsons and Cranston, 2005, 2006; Fraser et al., 2011). The introduction of lead into gasoline across the North American continent during the 1930s (Nriagu, 1990; Graney et al., 1995) may be apparent in the stable-lead enrichment profile after 15 cm, corresponding to a ^{210}Pb age of 1944 ± 3 CE. The decline in enrichment seen in the same profile at 10 cm (1979 ± 2 CE, ^{210}Pb age) is likely attributable to the fall in lead pollution due to new emissions regulations established in the early 1970s (Nriagu, 1990) and recorded widely throughout Canada (Blais, 1996). The post-bomb radiocarbon date from the same depth (10 cm) was calibrated to 1982 to 1985 CE and provides an additional and comparable age-depth constraint for these young sediments.

The age-depth modelling for SimVII incorporated the sequence

of radiocarbon ages and ^{210}Pb-derived ages from the monolith without the need for removing potential outliers (Fig. 8). Alongside trace metal enrichment factors, a micro-charcoal profile provided additional validation for the chronology. Onset and peak charcoal accumulation occurs across 38 to 32 cm depth, corresponding to modelled ages of 1647 ± 27 CE and 1731 ± 32 CE respectively. This epoch coincides with the onset of French settlement in Acadia and eventually the Gaspé and the Baie des Chaleurs regions from the early 1600s (Fauteux, 1948). Fishing villages became established (and were subsequently sacked and burned by the British) along the northern shore of the bay (e.g., at Percé and Pabos) from the 1690s (Mimeault, 2005). Timing of the charcoal peak at 32 cm coincides with the climactic exodus of Acadian refugees to the region and the settlement of nearby Bonaventure in 1760 CE following the Battle of Restigouche (Fergusson, 1955; Caron, 2015). The secondary charcoal peak at 21 cm depth (Fig. 6), corresponding to a modelled age of 1882 ± 10 CE, coincides with increased settlement in the region associated with the foundation of Saint-Siméon in 1869 CE. This event coincides with peaks in bulk density measurements across the marsh (Fig. 7), which are caused by a thin (2 cm) sand-rich lens in the lithostratigraphy, possibly relating to a sudden and short-lived influx of coarse grained sediment from either the catchment (e.g., from deforestation activity) or from the basin (e.g., from extreme wave conditions).

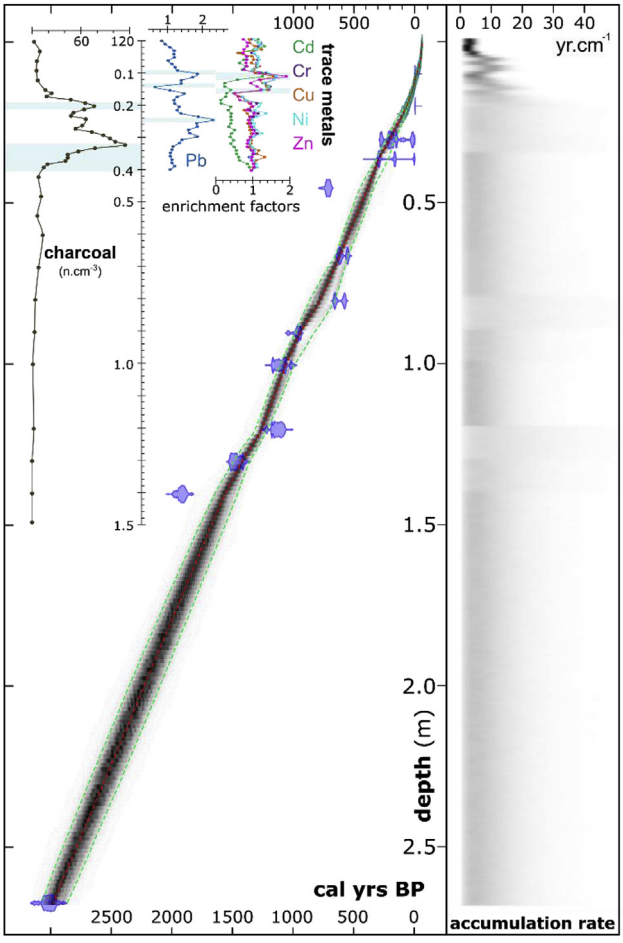

Fig. 8. Age-depth model for monolith SimVII. The mean (*dashed red*) and 2σ range (*dashed green*) of MCMC age-depth model iterations (*black shading*) are based on calibrated radiocarbon probability distribution functions (*blue*) and ^{210}Pb age-depth solutions (*green*). Microcharcoal counts and trace-metal profiles are presented with features highlighted for comparisons with the age-depth model. (For interpretation of the references to colour in this figure legend, the reader is referred to the Web version of this article.)

4.4. Quantitative sea-level reconstructions

Foraminifera assemblages from 0 to 37 cm and 70–135 cm in monolith SimVII had suitable modern analogues within the surface training set (Fig. 6). Samples from 37 to 70 cm contained no *in situ* populations of salt-marsh foraminifera and therefore lacked modern analogues suitable for validating their use in reconstructing sea level. The occasional foraminifera tests present in this unit may be storm-spray transported, as implied by the low abundance but highly abraded calcareous shells. Predictions of PMSEs for the remainder of the monolith had sample specific RMSEP uncertainties of between ±0.15 and 0.16 m, following conversion from SWLI values to elevations above local MSL at Saint-Siméon. Reconstructed PMSE values are relatively invariant between 135 and 70 cm depth. However, between 35 cm and the surface, phases of higher (~30 and 8 cm) and lower (~18 and 10 cm) PMSE values occur, which are replicated in the secondary reconstruction core, SimIV (Fig. 6b).

Compaction modelling results used to correct the estimates of RSL derived from sample PMSE values ± RMSEP values (Supplementary Material) estimated effective stress at the base of the monolith to 5.20 ± 0.12 kPa (Fig. 9). The estimated effective stress at the base of the intertidal deposits is 4.36 ± 0.11 kPa and estimated maximum values of σ'_y (1.25 kPa) are exceeded at depths greater than 0.46 m in the majority of model runs in the intertidal sediments. As such, these sediments are in their relatively high compressibility condition. In contrast, the greater values σ'_y specified for the lower freshwater peat are not exceeded in any model runs. In turn, greater PDL is observed in the upper intertidal deposits than in the lower freshwater peat. There is no PDL at the top and base of the monolith, with a distinct change in the shape of the PDL profile at the contact between the two key stratigraphic units. A curved PDL profile lacking sharp inflections within the intertidal stratum is evident, with maximum PDL of 0.10 ± 0.01 m at 79 cm, which is the approximate mid-point of the intertidal strata. There is greater uncertainty in the modelled effective stress profile for the lower freshwater peat deposit due to the greater uncertainty for LOI values within this unit. This effect propagates upwards into the PDL profile uncertainty in the intertidal deposits.

Reconstruction results reveal nearly 3 m of RSL rise at Saint-Siméon for the past ~3000 years (Fig. 10). Basal radiocarbon dates from the subsurface ligneous-rich peat, calibrated to −1084 ± 105 CE and −197 ± 139 CE, provide two non-compacted Late Holocene RSL constraints. The continuous salt-marsh based sea-level reconstruction extends from ~500 CE to present day with a data hiatus between ~1350 and 1650 CE. Validation for the record is provided in three forms: i) the surveyed elevation of the monolith top (0.77 m MSL) is reconstructed to within uncertainty by the PMSE of the top sample (0.64 ± 0.15 m MSL); ii) the second sea-level reconstruction from monolith SimIV shows similar RSL trends and magnitudes to the primary record for the past ~200 years (Fig. 10b), and; iii) recent sea-level estimates from the two reconstructions accord with nearby tide-gauge data from Belledune, New Brunswick (Fig. 10b). The replicate reconstructions for the past two centuries (Fig. 10b) improve confidence in our new record and demonstrate that higher resolution analyses (SimIV) may contribute addition detail, rather than noise, to reconstructed RSL trends.

The regression analysis of the data shows a near-linear secular trend of sea-level rise (Fig. 10c). The average of the secular trend mean rates from ~500 CE to present day is 0.93 mm yr^{-1}, with mean (2σ) uncertainties of ±1.25 mm yr^{-1}. The secular trend of the sea-level record is non-uniform and contains higher than average rates of rise that occur between 500 and 800 CE and during the two

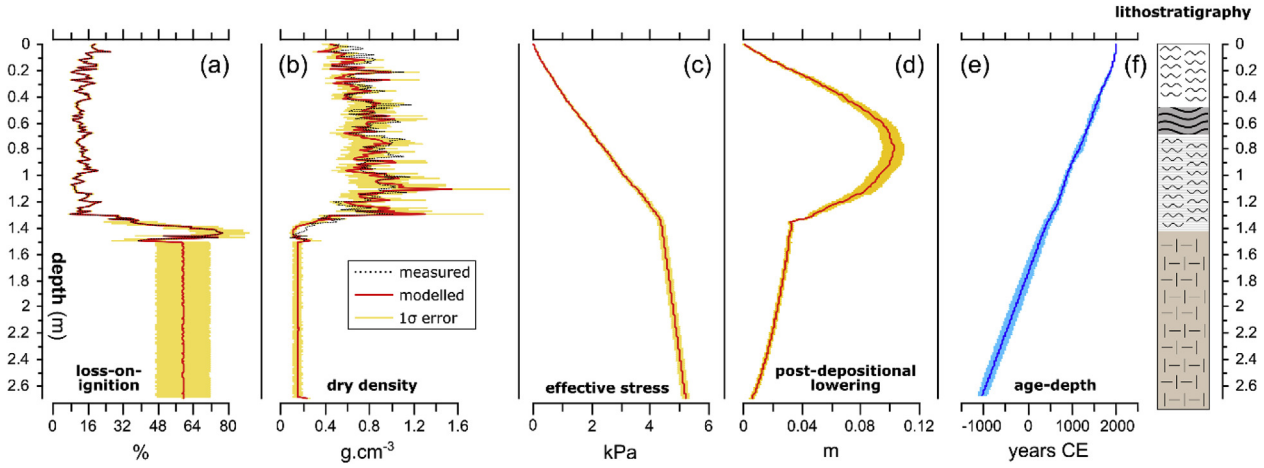

Fig. 9. Physical and geotechnical properties. Measured (*black dotted*) and modelled (*red*) ±1σ (*yellow*) results of (a) LOI, (b) dry bulk density, (c) effective stress and (d) PDL in monolith SimVII. (e) Age-depth model and (f) lithostratigraphy are also shown. . (For interpretation of the references to colour in this figure legend, the reader is referred to the Web version of this article.)

most recent centuries (Fig. 10d). The regression performed on the model residuals shows internal variability within the sea-level record (Fig. 10c). This structure occurs over broadly centennial time scales with mean rates that cycle between −1 and 1 mm yr^{-1} for before 1800 CE. The amplitude of this internal variability increases after 1800 CE. There are sustained periods of net acceleration between 1800 and 1900 CE and between 1950 CE and present day (Fig. 10d). Linear regression of the available tide gauge data and corresponding reconstructed trends of internal variability since 2000 CE show comparable rates of 4.7 mm yr^{-1} and 4.48 ± 2.19 mm yr^{-1} respectively, which exceed secular and internal variability rates over the past ~1500 years.

5. Discussion

The subsurface lithology at Saint-Siméon implies near-continuous transgression throughout the past ~3000 yrs. The basal clay unit with unconformable upper contact likely formed distally from the ice sheet in a glaciomarine setting, after ablation of the regional ice caps when the lithosphere was still depressed and a sea-level high stand was present throughout the bay (Rampton et al., 1984; Gray, 1987; Syvitski and Praeg, 1989; Veillette and Cloutier, 1993). Subsequent rebound of the lithosphere created RSL fall during the early Holocene to a low stand several tens of metres below present (Syvitski, 1992), after which gradual submergence took place throughout the Holocene in line with eustatic sea-level changes (Grant, 1970, 1975; 1977; Syvitski, 1992). The establishment of coastal peat deposits at Saint-Siméon provides the earliest evidence of recent transgression at the site. A rising groundwater table as a result of RSL encroachment can create favourable conditions for coastal peat formation (van de Plassche, 1982; van de Plassche et al., 2005) and has been recorded at locations throughout Québec (Garneau, 1997, 1998; Barnett et al., 2017a). Depending on hydraulic connectivity, freshwater coastal peats may form at around ±0.20 m to the level of mean high water (e.g., Berendsen et al., 2007; Barnett et al., 2017a). Conservatively, we use the dated onset of peat formation at Saint-Siméon as sea-level limiting points to define the maximum possible height of RSL at ~3000 yrs BP (Fig. 10).

5.1. Sediment dynamics and RSL changes

The sea-level reconstruction (Fig. 10) records the effects of combined local (e.g., sediment dynamics and sediment compaction), regional (e.g., isostatic and dynamic ocean) and extra-regional (e.g., ocean volume flux) drivers. At the local scale, accommodation space on the marsh surface created from an increase in sea-surface height or negative vertical land motion is infilled by sediment deposition that is driven by primary organic productivity at the surface and suspended sediment delivery from tidal inundation (Allen, 1990, 2000). Ongoing marsh accretion and infill of accommodation space in line with RSL rise is represented by preservation of the relative elevation of the surface, as depicted by invariant foraminifera assemblages. Accelerating RSL rise lowers the relative elevation of the marsh surface and is represented by a shift towards low-marsh taxa such as *M. fusca* (Fig. 6). In most instances, accumulation at the surface is able to keep pace with even rapid expansion of accommodation space due to enhanced biomass productivity of low-marsh flora and longer episodes of minerogenic sedimentation (Kirwan et al., 2016). The near constant sediment accumulation rate (0.95 ± 0.48 mm yr^{-1}) over the length of the record (Fig. 8) suggests that there has not been a hiatus in sediment delivery to the site. This reflects regional histories where sediment delivery to the St Lawrence Estuary has remained uninterrupted since the early Holocene (St-Onge et al., 2003). The deviation from salt-marsh typical accumulation across 1350 to 1650 CE is the only obvious example of a change in depositional environment and therefore we have not attempted to produce a precise sea-level reconstruction for this period.

Continuous RSL rise occurred throughout the Late Holocene, although our record has a data hiatus for the period ~1350 to ~1650 CE, across the Little Ice Age (LIA). This part of the record derives from 0.37 to 0.70 m in monolith SimVII where viable *in situ* populations of foraminifera and testate amoebae are absent. Diagenetic removal of organism tests can skew the stratigraphic record and may occur following RSL lowering and oxidation of salt-marsh sediments (Berkeley et al., 2007). However, the low concentration of agglutinated tests and rare presence of small and abraded calcareous forms suggests that diagenesis is an unlikely cause. Alternatively, foraminiferal absence can be explained by relative raising of the marsh surface, which would remove the site from the intertidal zone. Although the absence of testate amoebae, which are most abundant at supratidal elevations (Barnett et al., 2017b), and presence of freshwater $CaCO_3$ gastropod and bivalve shells both refute the development of a supratidal terrestrial environment. The gradual decline in foraminifera concentrations implies

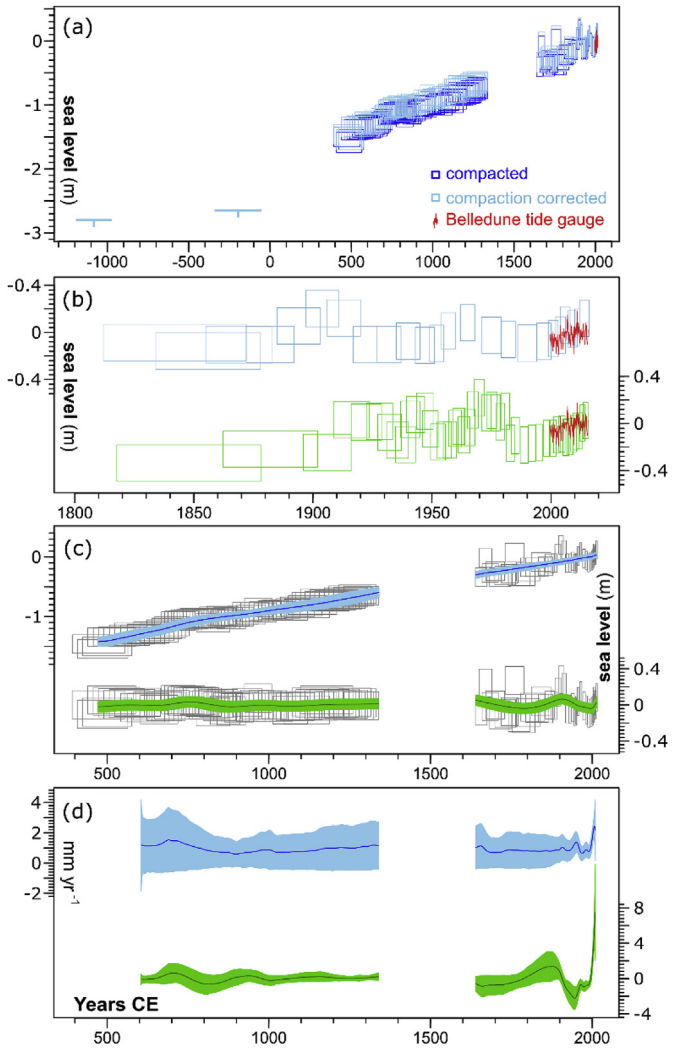

Fig. 10. Reconstructed sea-level data. (a) Late Holocene sea-level reconstruction data from monolith SimVII showing solutions prior to (*dark blue*) and posterior to (*light blue*) PDL modelling and compaction correction. Also shown are two basal sea-level index points from Saint-Siméon and the available tide-gauge data from Belledune, New Brunswick (*red*). (b) Validation reconstruction data from monolith SimIV (*green*) shown against the equivalent reconstruction data from monolith SimVII (*blue*) with tide-gauge data for comparison (*red*). (c) Estimation of the secular sea-level trend from monolith SimVII (*blue*) (±2σ) and of the residual 'internal variability' (*green*) (±2σ). (d) Calculated rates of change from the relative sea-level trends shown in (c). (For interpretation of the references to colour in this figure legend, the reader is referred to the Web version of this article.)

'freshening' of the site, and so a reduction in marine influence. Continued accumulation (Fig. 8) and relatively invariant organic and clastic content imply constant biomass production and infill of accommodation space. A plausible explanation is isolation of the site from tidal inundation, possibly caused by increased freshwater delivery and barrier development. Coastal ponding may explain the rare presence of *ex situ* foraminifera from, for example, reworking and delivery of small abraded calcareous forms via storm-spray. The continued development and infill of accommodation space implies gradual lowering of the accumulating surface, which is likely to have resulted from GIA-induced subsidence. Importantly, the absence of intertidal conditions for ~300 years also suggests that sea level is not rising relative to the accumulating surface over this period. The timing coincides with reductions in the rates of RSL rise along the northeast coastline of North America (Gehrels, 1999; Gehrels et al., 2002; Kemp et al., 2013, 2015, 2017a,b) and in a globally-averaged sea-level record (Kopp et al., 2016), concomitant with sea-level fall during the LIA (Grinstead et al., 2009). Holocene precipitation anomalies for Québec and Labrador were highest during the LIA (Viau and Gajewski, 2009), providing a mechanism that supports standing coastal water bodies during this period. Alternatively, extensive and longer lasting coastal- and sea-ice cover during the LIA, as suggested by modelling studies (e.g., Lehner et al., 2013) may also contribute to the freshening signal seen in the biostratigraphy for this time.

Sediment compaction from overburden compression (Allen, 2000) can alter the elevation of (palaeo-) marsh surfaces relative to sea level. Model-derived estimates of PDL throughout the monolith (Fig. 9) permitted assessment of the effects of local-scale sediment compaction on RSL changes. Regression analysis of the compacted and PDL-corrected reconstructions were compared to determine RSL changes driven by overburden compression at the site (Fig. 11). Comparison of the secular trends reveal that PDL contributes up to an additional 0.18 ± 0.27 mm yr^{-1} of equivalent RSL rise within the length of the record. The slowly varying rates of change captured by the secular trends contain the entire compaction-induced RSL signal as the difference between the estimates of internal variability for the compacted and the PDL-corrected records are negligible (Fig. 11).

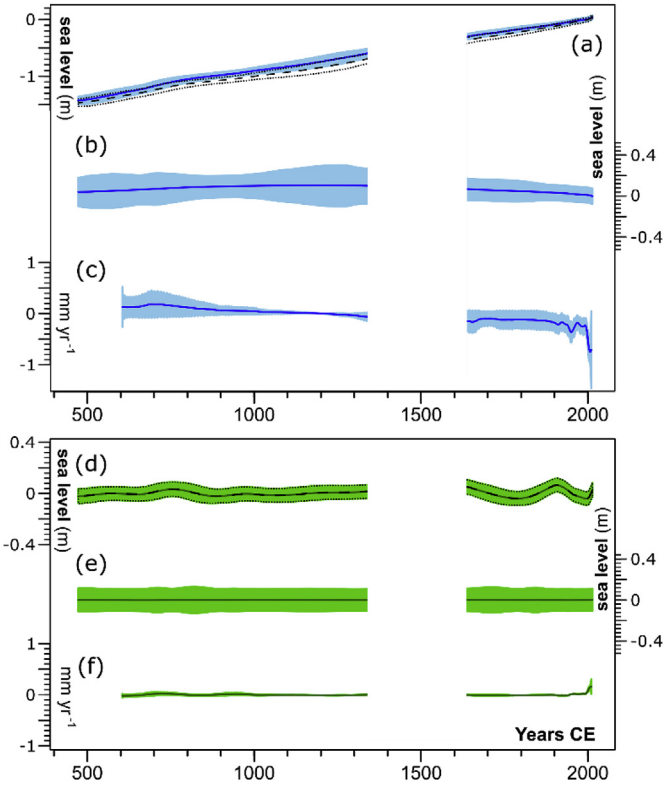

Fig. 11. Comparison of trends between compacted and PDL-corrected records. (a) Secular trends (±2σ) of the compacted (*black dabbled*) and PDL-corrected (*blue*) records. (b) Difference between compacted and PDL-corrected secular trends (±2σ). (c) Difference in calculated rates between compacted and PDL-corrected secular trends (±2σ). (d) Estimates of internal variability (±2σ) within the compacted (*black dabbled*) and PDL-corrected (*green*) records. (e) Difference between estimates of internal variability between the compacted and PDL-corrected records (±2σ). (f) Difference in calculated rates between the estimates of internal variability for the compacted and PDL-corrected records (±2σ). (For interpretation of the references to colour in this figure legend, the reader is referred to the Web version of this article.)

5.2. Secular RSL trends

The most recent velocity grid of vertical land motion for eastern Canada from the Canadian Spatial Reference System (CSRS) Precise Point Positioning (PPP), Natural Resources Canada resolves subsidence rates at Saint-Siméon to -0.39 ± 0.46 mm yr^{-1}, suggesting that GIA is responsible for much of the average mean secular rate (0.93 ± 1.25 mm yr^{-1}) for the past ~1500 years. Alternative GIA velocity models provide subsidence rates of -1.78 mm yr^{-1} (Koohzare et al., 2008; Didier et al., 2015) or greater (Peltier et al., 2015), which over-predict the rate of subsidence when compared against instrumental observation (Canadian Base Network, Natural Resources Canada) and secular RSL trends (this study). Modelled land motion rates have also been over-predicted for the Magdalen Islands in the Gulf of St Lawrence (Barnett et al., 2017a), but the new modern-day velocity grid from CSRS-PPP, Natural Resources Canada, provides an improvement to these model-data discrepancies.

A key feature within the long-term RSL trends at Saint-Siméon is the data hiatus between 1350 and 1650 CE that occurs during the LIA (1400–1700 CE; Mann et al., 2009). A similar record hiatus is evident in western Iceland across ~1300 to ~1600 CE (Gehrels et al., 2006; Saher et al., 2015), due also to reduced foraminifera content in the stratigraphy. Complete reconstructions of RSL change from the western North Atlantic reconstruct reduced rates of RSL rise across the period (or part of the period) ~1350 to ~1650 CE in Nova Scotia (Gehrels et al., 2005), Maine (Gehrels, 1999; Gehrels et al., 2002), Connecticut (Kemp et al., 2015), New York (Kemp et al., 2017a), New Jersey (Kemp et al., 2013) and North Carolina (Kemp et al., 2011, 2017b). Proposed mechanisms for multi-centennial RSL changes across this period (and throughout the Late Holocene) include steric effects (e.g., Gehrels et al., 2006) and changes in the strength of North Atlantic circulation (e.g., Kemp et al., 2015, 2017a). Disparities between the onsets and magnitudes of RSL phases along the North American eastern seaboard suggest the presence of spatio-temporal gradients of sea-level changes. These may be synonymous with patterns of change driven by AMOC variations. Acceleration in AMOC strength would cause RSL fall along the east coast of North America (Bingham and Hughes, 2009). However, this signal is most pronounced around Cape Hatteras (~35°N) and diminishes northward (Ezer, 2013), suggesting that the mechanism may not explain such sustained reductions in rates of RSL rise seen throughout the western North Atlantic. Indeed, persistent high-pressure atmospheric systems, increased sea-ice cover (Lehner et al., 2013) and freshening of the high-latitude North Atlantic (Moffa-Sánchez et al., 2014; Alonso-Garcia et al., 2017) were the likely cause of weakened ocean circulation during this period (Moreno-Chamarro et al., 2017), and therefore ocean-mass redistribution towards the North American continent.

The possible presence of a latitudinal gradient of RSL trends in the western North Atlantic across the LIA period warrants further attention. Southerly records from the North Atlantic reconstruct either no (Florida; Kemp et al., 2014) or very small (North Carolina, Kemp et al., 2011) downturns in rates of RSL rise. Further north at New Jersey, Connecticut and New York, rates of RSL rise are reduced, but still positive (Kemp et al., 2013, 2015, 2017a). Records from Maritime Canada document near-flat (Gehrels, 1999) or decreasing (Gehrels et al., 2002) RSL trends. Finally, the most northerly sites in western Iceland (Gehrels et al., 2006; Saher et al., 2015) and eastern Québec (this study) exhibit a disconnect between the accumulating marsh surface and 'normal' intertidal conditions, which is attributed (in this study at least) to lowered RSL. High-pressure atmospheric systems associated with persistent arctic air masses across the North Atlantic contributed to greater sea-level pressures during the LIA (Lehner et al., 2013). However, such a north-south gradient in RSL change amplitudes might also point to a polar-ice mechanism that caused greater RSL fall in northerly locations and reduced RSL fall at southerly locations within the North Atlantic. The global sea-level fingerprint associated with ice-melt from Antarctica (Mitrovica et al., 2001) suggests that southern- (Antarctic), rather than northern- (Greenland), hemisphere ice-dynamics would be the more likely driver if this was the case. An exploration of this hypothesis, however, would need to reconcile: i) disparities in the onsets and durations of RSL phases across the LIA from the different records; ii) the apparent absence of a RSL downturn during the LIA in the eastern North Atlantic, as demonstrated by two RSL records from Scotland (Barlow et al., 2014), and; iii) the fingerprints and role of alternative sea-level mechanisms (e.g., Greenland and glacier ice-storage, steric and dynamic ocean processes) that also operate across the period.

5.3. Internal RSL variability

Short-term internal variability within the record from Saint-Siméon contributes up to an additional 0.61 ± 0.46 mm yr^{-1} to the secular RSL trend prior to 1800 CE (Fig. 10d). Higher amplitude variability is apparent prior to 1000 CE and after 1700 CE. Local scale dynamics, such as sediment delivery, vegetation growth, or even ecological noise from the modern-analogue reconstruction process may explain short-lived accelerations in accretion rates at the marsh surface, which would be reconstructed as temporary inflexions in the rates of RSL rise. However, multidecadal to centennial variability is recognised in RSL reconstructions from the western North Atlantic and may also be explained by ocean-atmosphere dynamics (e.g., Saher et al., 2015; Kemp et al., 2018). Reconstructions and climate indices of the NAO (Trouet et al., 2009; Ortega et al., 2015), AMO (Wang et al., 2017) and ocean circulation (Rahmstorf et al., 2015) rarely extend beyond the past millennium. Comparisons with our sea-level reconstruction are therefore partially hindered, especially with the data hiatus across the LIA. However, all three mechanisms display multidecadal to multicentennial-phase periods and share teleconnections that influence sea level in the western North Atlantic (e.g., Trouet et al., 2012; Sallenger et al., 2012). Phases of NAO influence ocean gyre and circulation strength via wind stress (Marshall et al., 2001; McCarthy et al., 2015), which in turn affects ocean heat distribution in the North Atlantic (Delworth and Mann, 2000; McCarthy et al., 2015), realised as the multidecadal evolution of the AMO (Enfield et al., 2001; Wang et al., 2017). Direct correlations exist between sea level in the western North Atlantic and the decadal to centennial phases of the NAO (McCarthy et al., 2015; Woodworth et al., 2017). The NAO is also capable of driving sea-level changes indirectly via its relationship with the AMOC (Marshall et al., 2001; Trouet et al., 2012; Delworth and Zeng, 2016). Weakening of AMOC transport in the western North Atlantic reduces the baroclinic gradient between the centre and western edge of the North Atlantic gyre, redistributing ocean mass towards the east coast of North America (Bingham and Hughes, 2009; Ezer, 2013). This signal is also expected to transmit to within the Gulf of St. Lawrence (Bingham and Hughes, 2009).

Over the course of the reconstruction following the LIA, a gradual RSL acceleration is apparent throughout the 19th century (Fig. 12) that potentially coincides with the onset of AMOC weakening (Rahmstorf et al., 2015, Fig. 12f). Reduced AMOC can follow negative NAO (which is maybe apparent around 1750 CE; Fig. 12d) as a response to the teleconnections outlined above. However, North Atlantic freshening from land-based ice melt (Böning et al., 2016; Yang et al., 2016) and sea-ice decline (Sévellec et al., 2017) is also a valid mechanism that may weaken ocean circulation and cause ocean mass redistribution towards the North American continent. The observed RSL acceleration also

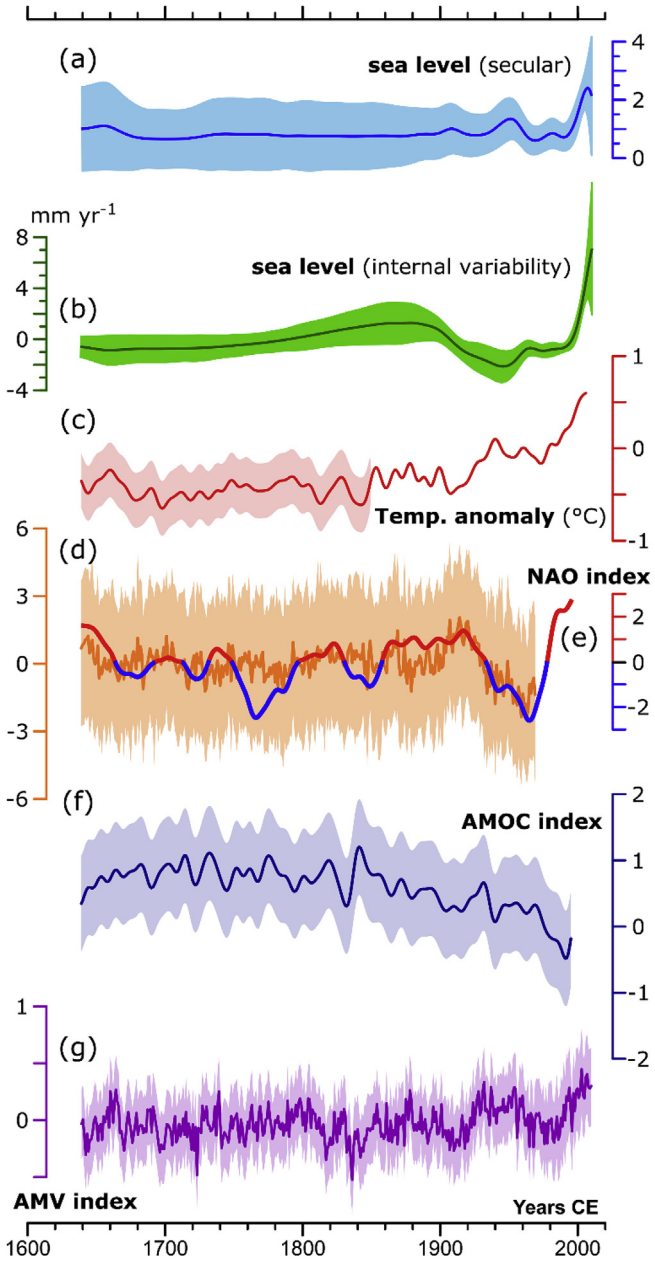

Fig. 12. Sea-level changes and climate indices following the Little Ice Age. Rates of change for the (a) secular trend and (b) estimate of internal variability at Saint-Siméon after 1600 CE. (c) Reconstruction of Northern Hemisphere temperature anomalies (±2σ) (after Mann et al., 2008); the disappearance of uncertainty estimates reflects the transition from reconstructed to instrumentally recorded temperatures. (d) Ensemble (±2σ) (after Ortega et al., 2015) and (e) bi-proxy (after Trouet et al., 2009) reconstructions of the North Atlantic Oscillation showing phase trends about reconstruction means. (f) Temperature-based reconstruction (±2σ) of the Atlantic Meridional Overturning Circulation (after Rahmstorf et al., 2015). (g) Ensemble reconstruction (±2σ) of Atlantic Multidecadal Variability (after Wang et al., 2017), which is used here to demonstrate phase periods of the Atlantic Multidecadal Oscillation.

coincides with increasing contributions from glaciers to global mean sea-level rise (Leclercq et al., 2011), although difficulties remain in defining glacier mass balance prior to 1900 CE (e.g., Marzeion et al., 2015; Zemp et al., 2015). A multidecadal RSL deceleration occurs over 1900 CE and follows a temporary positive phase in NAO indices (Fig. 12d and e). Correlations between NAO phase and North Atlantic sea-level changes are already well evidenced from tide gauge data and salt-marsh-based sea-level reconstructions (Saher et al., 2015; Woodworth et al., 2017). However, this feature is short-lived prior to sustained RSL acceleration after 1950 CE, which coincides with Northern Hemisphere (Fig. 12c; Mann et al., 2008) and North Atlantic (Fig. 12g; Wang et al., 2017) warming, AMOC deterioration (Fig. 12f) and weakened NAO (Fig. 12d and e).

Despite possible correlations between RSL trends and ocean-atmosphere processes, distinguishing causative mechanisms remains a challenge. Sea-level changes in this region of study appear to contain multiple phases of acceleration following the LIA, which may contrast with existing records from the western North Atlantic that highlight a single acceleration occurring towards the end of the 19th century (Kemp et al., 2015, 2017a,b and references within) or later during the beginning of the 20th century (Gehrels and Woodworth, 2013). There is a need for tighter constraints on the mass flux between the oceans and the cryosphere following the LIA, which will support further comparisons between mechanisms that drive ocean volume changes versus those that redistribute ocean mass. The timings and potential sea-level equivalent contributions of the relevant mechanisms will be key in determining the impacts that regional processes have had in the build up to unprecedented 21st century sea-level rise and for better constraining estimates of future sea-level rise.

6. Conclusions

Salt-marsh foraminifera have been used to reconstruct a relative sea-level history at Saint-Siméon (eastern Québec) for the past ~ three millennia. Basal, marine-limiting sea-level index points indicate that RSL rose from −3 m to −1.5 m relative to present day between −1000 and 500 yrs CE. Between 500 CE and present day, RSL rose at a mean secular rate of 0.93 ± 1.25 mm yr^{-1}. Negative vertical land motion is a significant contributor to this secular rate of rise for the past ~1500 years. However, modern day velocity measurements for the region (e.g., Peltier et al., 2015) still overpredict the rate of land subsidence in the Baie des Chaleurs (this study) and elsewhere in the Gulf of St. Lawrence (Barnett et al., 2017a). Sediment compaction also contributed a long-term geophysical signal to the secular trend, which has been accounted for in this study by using a geotechnical model to estimate post-depositional lowering of the sediments used to reconstruct sea level. The rate of secular RSL rise is not uniform over the studied period and higher than average rates of rise occurred between 500 and 800 CE and after 1900 CE. A data hiatus also occurs in the record between ~1350 and 1650 CE, which coincides with the timing of the LIA. This data hiatus is attributed to a lowered RSL creating a disconnect between the accumulating marsh surface and tidal inundation. Sea-level records from the northwestern North Atlantic (Gehrels, 1999; Gehrels et al., 2002, 2006; Kemp et al., 2013, 2015, 2017a; Saher et al., 2015; this study) indicate that a lowered RSL during the LIA might point to an ice-loaded Antarctica for this period, although distinguishing between this and concomitant signals from, e.g., Greenland and glacier ice masses remains a challenge. An estimate of the internal structure within the secular residuals of the 1500 year RSL record indicates that short-term, higher-frequency variability can contribute additional RSL rise on the order of ~0.5–2 mm yr^{-1} over multidecadal to centennial scales. This variability shares frequencies with climate indices such as the NAO and AMV and phases of ocean circulation (AMOC). Positive attribution of ocean-atmosphere sea-level drivers and variable RSL rates in the western North Atlantic remains an important research undertaking for the near future.

Data availability

Data supporting this publication are openly available from the University of Exeter institutional repository at https://doi.org/10.24378/exe.903.

Author contributions

RLB, PB, MG devised the study and carried out fieldwork. RLB carried out laboratory with SH and NS. RLB and DBS carried out statistical analyses. RLB and DJC wrote the paper with comments and assistance from all authors.

Acknowledgements

Financial support for this study was provided by the Québec Government as part of its program for natural-risk prevention and a Research Fellowship at the University of Exeter. MJB was funded by ICL Fertilisers. We acknowledge Christen Fraser, Pierre Rousseau and Jean-Pierre Castonguay Bélanger of the Univeristé du Québec à Rimouski for extensive assistance in the field and Catherine Robin at Natural Resources Canada for assistance with the NRCan velocity grid model. This is a contribution to PALSEA2 and IGCP Project 639.

Appendix A. Supplementary Material

Supplementary Material for this article can be found online at https://doi.org/10.1016/j.quascirev.2018.10.039.

References

Alcock, F.J., 1935. Geology of the Chaleur Bay Region. Geological Survey of Canada. Memoir 183.
Allen, J.R.L., 1990. Constraints on measurement of sea-level movements from salt-marsh accretion rates. J. Geol. Soc. 147, 5–7.
Allen, J.R.L., 2000. Morphodynamics of Holocene salt marshes: a review sketch from the Atlantic and southern north sea coasts of Europe. Quat. Sci. Rev. 19 (12), 1155–1231.
Alonso-Garcia, M., Kleiven, H.F., McManus, J.F., Moffa-Sanchez, P., Broecker, W.S., Flower, B.P., 2017. Freshening of the labrador sea as a trigger for little ice age development. Clim. Past 13, 317–331.
Appleby, P.G., 2001. Chronostratigraphic techniques in recent sediments. In: Last, W.M., Smol, J.P. (Eds.), Tracking Environmental Change Using Lake Sediments. Volume 1: Basin Analysis, Coring and Chronological Techniques. Kluwer Academic Publishers, Dordrecht, Netherlands.
Bail, P., 1985. Un mouvement glaciaire vers le nord-ouest dans la région de Saint-Godefroi, Gaspésie, Québec. Can. J. Earth Sci. 22, 1871–1876.
Ball, D.F., 1964. Loss on ignition as an estimate of organic matter and organic carbon in non-calcareous soil. J. Soil Sci. 15, 84–92.
Barber, K.E., Chambers, F.M., Maddy, D., Stoneman, R., Brew, J.S., 1994. A sensitive high resolution record of late Holocene climatic change from a raised bog in northern England. Holocene 4, 198–205.
Barlow, N.L.M., Long, A.J., Saher, M.H., Gehrels, W.R., Garnett, M.H., Scaife, R.G., 2014. Salt-marsh reconstructions of relative sea-level change in the North Atlantic during the last 2000 years. Quat. Sci. Rev. 99, 1–16.
Barlow, N.L.M., Shennan, I., Long, A.J., Gehrels, W.R., Saher, M.H., Woodroffe, S.A., Hillier, C., 2013. Salt marshes as late Holocene tide gauges. Global Planet. Change 106, 90–110.
Barnett, R.L., Bernatchez, P., Garneau, M., Juneau, M.-N., 2017a. Reconstructing late Holocene relative sea-level changes at the Magdalen Islands (Gulf of St. Lawrence, Canada) using multi-proxy analyses. J. Quat. Sci. 32 (3), 380–395.
Barnett, R.L., Garneau, M., Bernatchez, P., 2016. Salt-marsh sea-level indicators and transfer function development for the Magdalen Islands in the Gulf of St. Lawrence, Canada. Mar. Micropaleontol. 122, 13–26.
Barnett, R.L., Gehrels, W.R., Charman, D.J., Saher, M.H., Marshall, W.A., 2015. Late Holocene sea-level change in arctic Norway. Quat. Sci. Rev. 107, 214–230.
Barnett, R.L., Newton, T.L., Charman, D.J., Gehrels, W.R., 2017b. Salt-marsh testate amoebae as precise and widespread indicators of sea-level change. Earth Sci. Rev. 164, 193–207.
Berendsen, H.J.A., Makaske, B., van de Plassche, O., van Ree, M.H.M., Das, S., van Dongen, M., Plouman, S., Schoenmakers, W., 2007. New groundwater-level rise data from the Rhine-Meuse Delta - implications for the reconstruction of Holocene relative mean sea-level rise and differential land-level movements. Neth. J. Geosci. 86, 333–354.
Berkeley, A., Perry, C.T., Smithers, S.G., Horton, B.P., Taylor, K.G., 2007. A review of the ecological and taphonomic controls on foraminiferal assemblage development in intertidal environments. Earth Sci. Rev. 83, 205–230.
Bertler, N.A.N., Mayewski, P.A., Carter, I., 2011. Cold conditions in Antarctica during the Little Ice Age – implications for abrupt climate change mechanisms. Earth Planet Sci. Lett. 308, 41–51.
Bernatchez, P., 2003. Évolution littorale holocène et actuelle des complexes deltaiques de Betsiamites et de Manicouagan-Outardes: synthèse, processus, causes et perspectives. Département de géographie. Université Laval, Québec.
Bingham, R.J., Hughes, C.W., 2009. Signature of the Atlantic meridional overturning circulation in sea level along the east coast of North America. Geophys. Res. Lett. 36 https://doi.org/10.1029/2008GL036215.
Birks, H.J.B., 1995. Quantitative palaeoenvironmental reconstructions. In: Maddy, D., Brew, J.S. (Eds.), Statistical Modelling of Quaternary Science Data. Quaternary Research Association, Cambridge, pp. 161–253.
Birks, H.J.B., Line, J.M., Juggins, S., Stevenson, A.C., ter Braak, C.J.F., 1990. Diatoms and pH reconstruction. Phil. Trans. Roy. Soc. Lond. B 327, 263–278.
Blaauw, M., Christen, A.J., 2011. Flexible paleoclimate age-depth models using an autoregressive gamma process. Bayesian Anal. 6, 457–474.
Blais, J.M., 1996. Using isotopic tracers in lake sediments to assess atmospheric transport of lead in eastern Canada. Water Air Soil Pollut. 92, 329–342.
Böhm, E., Lippold, J., Gutjahr, M., Frank, M., Blaser, P., Antz, B., Fohlmeister, J., Frank, N., Andersen, M.B., Deininger, M., 2015. Strong and deep Atlantic meridional overturning circulation during the last glacial cycle. Nature 517, 73–76.
Böning, C.W., Behrens, E., Biastoch, A., Getzlaff, K., Bamber, J.L., 2016. Emerging impact of Greenland meltwater on deepwater formation in the North Atlantic Ocean. Nat. Geosci. 9, 523–527.
Bradley, S.L., Milne, G.A., Horton, B.P., Zong, Y., 2016. Modelling sea level data from China and Malay-Thailand to estimate Holocene ice-volume equivalent sea level change. Quat. Sci. Rev. 137, 54–68.
Brain, M.J., 2015. Compaction. In: Shennan, I., Long, A.J., Horton, B.P. (Eds.), Handbook of Sea-level Research. Wiley, Chichester, pp. 452–469.
Brain, M.J., 2016. Past, present and future perspectives of sediment compaction as a driver of relative sea level and coastal change. Curr. Clim. Change Rep. 1–11.
Brain, M.J., Kemp, A.C., Hawkes, A.D., Engelhart, S.E., Vane, C.H., Cahill, N., Hill, T.D., Donnelly, J.P., Horton, B.P., 2017. Exploring mechanisms of compaction in salt-marsh sediments using Common Era relative sea-level reconstructions. Quat. Sci. Rev. 167, 96–111.
Brain, M.J., Kemp, A.C., Horton, B.P., Culver, S.J., Parnell, A.C., Cahill, N., 2015. Quantifying the sediment compaction to late Holocene salt-marsh sea-level reconstructions, North Carolina, USA. Quat. Res. 83 (1), 41–51.
Brain, M.J., Long, A.J., Petley, D.N., Horton, B.P., Allison, R.J., 2011. Compression behaviour of minerogenic low energy intertidal sediments. Sediment. Geol. 233 (1–4), 28–41.
Brain, M.J., Long, A.J., Woodroffe, S.A., Petley, D.N., Milledge, D.G., Parnell, A.C., 2012. Modelling the effects of sediment compaction on salt marsh reconstructions of recent sea-level rise. Earth Planet Sci. Lett. 345–348, 180–193.
Brisebois, D., 1981. Géologie de la région de Gaspé. Ministère de l'Énergie et des Ressources du Québec. DPV-824.
Brookes, I.A., Scott, D.B., McAndrews, J.H., 1985. Postglacial relative sea-level change, port au port areas, west Newfoundland. Can. J. Earth Sci. 22, 1039–1047.
Bryden, H.L., King, B.A., McCarthy, G.D., McDonagh, E.L., 2014. Impact of a 30% reduction in Atlantic meridional overturning during 2009-2010. Ocean Sci. 10, 683–691.
Cahill, N., Kemp, A.C., Horton, B.P., Parnell, A.C., 2015. Modeling sea-level change using errors-in-variables integrated Gaussian processes. Annu. Appl. Stat. 9 (2), 547–571.
Callard, S.L., Gehrels, W.R., Morrison, B.V., Grenfell, H.R., 2011. Suitability of salt-marsh foraminifera as proxy indicators of sea level in Tasmania. Mar. Micropaleontol. 79, 121–131.
Campbell, I.D., 1996. Power function for interpolating dates in recent sediments. J. Paleolimnol. 15, 107–110.
Caron, C.-I., 2015. The Acadians. The Canadian Historical Association, Ottawa. Booklet No. 3.
Christen, J.A., Pérez, E.S., 2009. A new robust statistical model for radiocarbon data. Radiocarbon 51, 1047–1059.
Clark, J.S., Royall, P.D., 1996. Local and regional sediment charcoal evidence for fire regimes in presettlement north-eastern North America. J. Ecol. 84 (3), 365–382.
Collin, A., Long, B., Archambault, P., 2010. Salt-marsh characterization, zonation assessment and mapping through dual-wavelength LiDAR. Remote Sens. Environ. 114, 520–530.
Corbett, D.R., Walsh, J.P., 2015. ^{210}Lead and ^{137}Cesium: establishing a chronology for the last century. In: Shennan, I., Long, A.J., Horton, B.P. (Eds.), Handbook of Sea-level Research. Wiley, Chichester, pp. 361–372.
Cunningham, S.A., Kanzow, T., Rayner, D., Baringer, M.O., Johns, W.E., Marotzke, J., Longworth, H.R., grant, E.M., Hirschi, J.J.-M., Beal, L.M., Meinen, C.S., Bryden, H.L., 2007. Science 317, 935–938.
Curry, R.G., McCartney, M.S., Joyce, T.M., 1998. Oceanic transport of subpolar climate signals to mid-depth subtropical waters. Nature 391, 575–577.
Daly, J.F., Belknap, D.F., Kelley, J.T., Bell, T., 2007. Late Holocene sea-level change around Newfoundland. Can. J. Earth Sci. 44, 1453–1465.
Delworth, T.L., Mann, M.E., 2000. Observed and simulated multidecadal variability in the Northern Hemisphere. Clim. Dynam. 16, 661–676.
Delworth, T.L., Zeng, F., 2016. The impact of the north Atlantic oscillation on climate through its influence on the Atlantic meridional overturning circulation. J. Clim.

29, 941–962.
de Vernal, A., Hillaire-Marcel, C., 2006. Provincialism in trends and high frequency changes in the northwest North Atlantic during the Holocene. Global Planet. Change 54, 263–290.
Didier, D., Bernatchez, P., Boucher-Brossard, G., Lambert, A., Fraser, C., Barnett, R.L., van-Wierts, S., 2015. Coastal flood assessment based on field debris measurements and wave runup empirical model. J. Mar. Sci. Eng. 3, 560–590.
Dionne, J.-C., 1985. Observations sur le Quaternaire de la rivière Boyer, côte sud de l'estuaire du Saint-Laurent, Québec. Géogr. Phys. Quaternaire 39 (1), 35–46.
Dionne, J.-C., 1990. Observations sur le niveau marin relatif à l'Holocène, à Rivière-du-Loup, estuaire du Saint- Laurent, Québec. Géogr. Phys. Quaternaire 44 (1), 45–53.
Dionne, J.-C., 1996. La terrasse Mitis à la pointe aux Alouettes, côte nord du moyen estuaire du Saint-Laurent, Québec. Géogr. Phys. Quaternaire 50 (1), 57–72.
Dionne, J.-C., 1997. Nouvelles données sur la transgression Laurentienne, côte sud du moyen estuaire du Saint- Laurent, Québec. Géogr. Phys. Quaternaire 51 (2), 201–210.
Dionne, J.-C., 1999. Indices de fluctuations mineures du niveau marin relatif à l'Holocène supérieur, à L'Isle-Verte, côte sud de l'estuaire du Saint-Laurent, Québec. Géogr. Phys. Quaternaire 53 (2), 277–285.
Dionne, J.-C., 2001. Relative sea-level changes in the St. Lawrence estuary from deglaciation to present day. In: Weddle, T.K., Retelle, M.J. (Eds.), Deglacial History and Relative Sea-level Changes, Northern New England and Adjacent Canada. Geological Society of America, Denver, pp. 271–284.
Dionne, J.-C., 2002. Une nouvelle courbe du niveau marin relatif pour la région de Rivière-du-Loup (Québec). Géogr. Phys. Quaternaire 56 (1), 33–44.
Dionne, J.-C., 2004. Âge et taux moyen d'accrétion verticale des schorres du Saint-Laurent estuarien, en particulier ceux de Montmagny et de Sainte-Anne-de-Beaupré, Québec. Géogr. Phys. Quaternaire 58 (1), 73–108.
Dionne, J.-C., Coll, D., 1995. Le niveau marin relatif dans la région de Matane (Québec), de la déglaciation à nos jours. Géogr. Phys. Quaternaire 49 (3), 363–380.
Dionne, J.-C., Occhietti, S., 1996. Aperçu du Quaternaire à l'embouchure du Saguenay, Québec. Géogr. Phys. Quaternaire 50 (1), 5–34.
Dubois, J.M.M., Gwyn, Q.H.J., Gratton, D., Painchaud, A., Perras, S., Cadieux, R., Saint-Pierre, L., Bigras, P., 1985. Géologie des formations en surface et géomorphologie de l'île d'Anticosti, Québec. Geological Survey of Canada, A Series Map no, p. 1660A.
Dyke, A.S., 2004. An outline of North American deglaciation with emphasis on central and northern Canada. Dev. Quat. Sci. 2, 373–424.
Dyke, A.S., Peltier, W.R., 2000. Forms, response times and variability of relative sea-level curves, glaciated North America. Geomorphology 32, 315–333.
Edwards, R.J., Wright, A.J., 2015. Foraminifera. In: Shennan, I., Long, A.J., Horton, B.P. (Eds.), Handbook of Sea-level Research. Wiley, Chichester, pp. 191–217.
El-Daoushy, F., Olsson, K., Garcia-Tenorio, R., 1991. Accuracies in Po-210 determination for lead-210 dating. Hydrobiologica 214, 43–52.
Enfield, D.B., Mestas, Nunez, A.M., Trimble, P.J., 2001. The Atlantic Multidecadal Oscillation and its relation to rainfall and river flows in the continental US. Geophys. Res. Lett. 28, 2077–2080.
Ezer, T., 2013. Sea level rise, spatially uneven and temporally unsteady: why the U.S. East Coast, the global tide gauge record, and the global altimeter data show different trends. Geophys. Res. Lett. 40, 5439–5444.
Fauteux, A., 1948. In: Stewart, W. (Ed.), The Encyclopaedia of Canada. University Associates of Canada, Toronto, pp. 192–202. Québec.
Fegyveresi, J.M., Alley, R.B., Fitzpatrick, J.J., Cuffey, K.M., McConnell, J.R., Voigt, D.E., Spencer, M.K., Stevens, N.T., 2016. Five millennia of surface temperatures and ice core bubble characteristics from the WAIS Divide deep core, West Antarctica. Paleoceanography 31, 416–433.
Fergusson, C.B., 1955. The expulsion of the Acadians. Dalhous. Rev. Halifax 35 (2).
Fraser, M., Surette, C., Vaillancourt, C., 2011. Spatial and temporal distribution of heavy metal concentrations in mussels (*Mytilus edulis*) from the Baie des Chaleurs, New Brunswick, Canada. Mar. Pollut. Bull. 62 (6), 1345–1351.
Frankel, L., Crowl, G.H., 1961. Drowned forests along the eastern coast of Prince Edward Island, Canada. J. Geol. 69, 352–357.
Flynn, W., 1968. The determination of low levels of polonium-210 in environmental materials. Anal. Chim. Acta 43, 221–227.
Garneau, M., 1997. Paléoécologie d'un secteur riverain de la rivière Saint-Charles: analyse macrofossile du site archéologique de la Grande Place, à Québec. Géogr. Phys. Quaternaire 51 (2), 211–220.
Garneau, M., 1998. Paléoécologie d'une tourbière littorale de l'estuaire maritime du Saint Laurent, Isle-Verte, Québec. Commission géologique du Canada. Bulletin 514.
Gehrels, W.R., 1999. Middle and late Holocene sea-level changes in eastern Maine reconstructed from foraminiferal salt marsh stratigraphy and AMS 14C dates on basal peat. Quat. Res. 52, 350–359.
Gehrels, W.R., 2002. Intertidal foraminifera as palaeoenvironmental indicators. In: Haslett, S.K. (Ed.), Quaternary Environmental Micropalaeontology. Oxford University Press, London/New York.
Gehrels, W.R., Kirby, J.R., Prokoph, A., Newnham, R.M., Achterberg, E.P., Evans, H., Black, S., Scott, D.B., 2005. Onset of recent rapid sea-level rise in the western Atlantic Ocean. Quat. Sci. Rev. 24, 2083–2100.
Gehrels, W.R., Belknap, D.F., Black, S., Newnham, R.M., 2002. Rapid sea-level rise in the Gulf of Maine, USA, since AD 1800. Holocene 14 (4), 383–389.
Gehrels, W.R., Marshall, W.A., Gehrels, M.J., Larsen, G., Kirby, J.R., Eiriksson, J., Heinemeir, J., Shimmield, R., 2006. Rapid sea-level rise in the North Atlantic Ocean since the first half of the nineteenth century. Holocene 16 (7), 949–965.
Gehrels, W.R., Milne, G.A., Kirby, J.R., Patterson, R.T., Belknap, D.F., 2004. Late Holocene sea-level changes and isostatic crustal movements in Atlantic Canada. Quat. Int. 120, 79–89.
Gehrels, W.R., van de Plassche, O., 1999. The use of *Jadammina macrescens* (Brady) and *Balticammina pseudomacrescens* Brönnimann, Lutze and Whittaker (Protozoa: Foraminiferida) as sea-level indicators. Palaeogeogr. Palaeoclimatol. Palaeoecol. 149, 89–101.
Gehrels, W.R., Woodworth, P.L., 2013. When did modern rates of sea-level rise start? Global Planet. Change 100, 263–277.
Graney, J.R., Halliday, A.N., Keeler, G.J., Nriagu, J.O., Robbins, J.A., Norton, S.A., 1995. Isotopic record of lead pollution in lake sediments from the northeastern United States. Geochim. Cosmochim. Acta 59 (9), 1715–1728.
Grant, D.R., 1970. Recent coastal submergence of the maritime provinces, Canada. Can. J. Earth Sci. 7, 676–689.
Grant, D.R., 1975. Recent coastal submergence of the maritime provinces. Proc. Nova Scotian Inst. Sci. 27 (3), 83–102.
Grant, D.R., 1977. Glacial style and ice limits, the Quaternary stratigraphic record, and changes of land and ocean level in the Atlantic Provinces, Canada. Géogr. Phys. Quaternaire 31, 247–260.
Gray, J.T., 1987. Quaternary Processes and Paleoenvironments in the Gaspé Peninsula and the Lower St. Lawrence Valley. XII[th] INQUA Congress Excursion Guide. Book C-4.
Grinstead, A., Moore, J.C., Jevrejeva, S., 2009. Reconstructing sea level from paleo and projected temperatures 200 to 2100AD. Clim. Dynam. https://doi.org/10.1007/s00382-008-0507-2.
Han, G., Ma, Z., Bao, H., Slangen, A., 2014. Regional differences of relative sea level changes in the Northwest Atlantic: historical trends and future projections. J. Geophys. Res.: Oceans 119, 156–164.
Hall, I.R., Bianchi, G.G., Evans, J.R., 2004. Centennial to millennial scale Holocene climate-deep water linkage in the North Atlantic. Quat. Sci. Rev. 23, 1529–1536.
Hastie, T., Tibshirani, R.J., 1986. Generalized additive models (with discussion). Stat. Sci. 1, 297–318.
Hastie, T., Tibshirani, R.J., 1990. Generalized Additive Models. Chapman & Hall, London.
Hildebrand, L.P., 1984. An assessment of environmental quality in the Baie des Chaleurs. Surveillance Report. Environment Canada. EPS-5-AR-84-8.
Hobbs, N.B., 1986. Mire morphology and the properties and behaviour of some British and foreign peats. Q. J. Eng. Geol. Hydrogeol. 19, 7–80.
Horton, B.P., Edwards, R.J., 2006. Quantifying Holocene Sea Level Change Using Intertidal Foraminifera: Lessons from the British Isles, vol 40. Cushman Foundation for Foraminiferal Research, Special Publication, pp. 0–97.
Horton, B.P., Edwards, R.J., Lloyd, J.M., 1999. UK intertidal foraminifera distributions: implications for sea-level studies. Mar. Micropaleontol. 36, 205–223.
Horton, B.P., Shennan, I., 2009. Compaction of Holocene strata and the implications for relative sealevel change on the east coast of England. Geology 37, 1083–1086.
Hua, Q., Barbetti, M., 2004. Review of tropospheric bomb ^{14}C data for carbon cycle modelling and age calibration purposes. Radiocarbon 46, 1273–1298.
Juggins, S., 2003. C2: a Microsoft Windows Program for Developing and Applying Palaeoecological Transfer Functions and for Visualising Multi-proxy Stratigraphic Datasets, 7.2. University of Newcastle, Newcastle Upon Tyne.
Juggins, S., 2015. rioja: analysis of quaternary science data, R package version 0.9-9. http://cran.r-project.org/package=rioja.
Kemp, A.C., Bernhardt, C.E., Horton, B.P., Kopp, R.E., Vane, C.H., Peltier, W.R., Hawkes, A.D., Donnelly, J.P., Parnell, A.C., Cahill, N., 2014. Late Holocene sea- and land-level change on the U.S. southeastern Atlantic coast. Mar. Geol. 357, 90–100.
Kemp, A.C., Hawkes, A.D., Donnelly, J.P., Vane, C.H., Horton, B.P., Hill, T.D., Anisfeld, S.C., Parnell, A.C., Cahill, N., 2015. Relative sea-level change in Connecticut (USA) during the last 2200 yrs. Earth Planet Sci. Lett. 428, 217–229.
Kemp, A.C., Hill, T.D., Vane, C.H., Cahill, N., Orton, P.M., Talke, S.A., Parnell, A.C., Sanborn, K., Hartig, E.K., 2017a. Relative sea-level trends in New York City during the past 1500 years. Holocene. https://doi.org/10.1177/0959683616683263.
Kemp, A.C., Horton, B.P., Donnelly, J.P., Mann, M.E., Vermeer, M., Rahmstorf, S., 2011. Climate related sea-level variations over the past two millennia. Proc. Natl. Acad. Sci. Unit. States Am. 108 (27), 11017–11022.
Kemp, A.C., Horton, B.P., Vane, C.H., Bernhardt, C.E., Corbett, D.R., Engelhart, S.E., Anisfeld, S.C., Parnell, A.C., Cahill, N., 2013. Sea-level change during the last 2500 years in New Jersey, USA. Quat. Sci. Rev. 81, 90–104.
Kemp, A.C., Kegel, J.J., Culver, S.J., Barber, D.C., Mallinson, D.J., Leorri, E., Bernhardt, C.H., Cahill, N., Riggs, S.R., Woodson, A.L., Mulligan, R.P., Horton, B.P., 2017b. Extended late Holocene relative sea-level histories for North Carolina, USA. Quat. Sci. Rev. 160, 13–30.
Kemp, A.C., Telford, R.J., 2015. Transfer functions. In: Shennan, I., Long, A.J., Horton, B.P. (Eds.), Handbook of Sea-level Research. Wiley, Chichester, pp. 470–499.
Kemp, A.C., Wright, A.J., Edwards, R.J., Barnett, R.L., Brain, M.J., Kopp, R.E., Cahill, N., Horton, B.P., Charman, D.J., Hawkes, A.D., Hill, T.D., van de Plassche, O., 2018. Relative sea-level change in Newfoundland, Canada during the past ~3000 years. Quat. Sci. Rev. 201, 89–10.
Kirwan, M.L., Temmerman, S., Skeehan, E.E., Guntenspergen, G.R., Fagherazzi, S., 2016. Overestimation of marsh vulnerability to sea level rise. Nat. Clim. Change 6, 253–260.

Klaminder, J., Renberg, I., Bindler, R., 2003. Isotopic trends and background fluxes of atmospheric lead in northern Europe: analyses of three ombotrophic bogs from south Sweden. Global Biogeochem. Cycles 17 (1). https://doi.org/10.1029/2002GB001921.
Kotler, E., Martine, R.E., Liddell, W.D., 1992. Experimental analysis of abrasion and dissolution resistance of modern reef-dwelling foraminifera: implications for the preservation of biogenic carbonate. Palaios 7 (3), 244–276.
Koozhare, A., Vaníček, P., Santos, M., 2008. Pattern of recent vertical crustal movements in Canada. J. Geodyn. 45, 133–145.
Kopp, R.E., Kemp, A.C., Bittermann, K., Horton, B.P., Donnelly, J.P., Gehrels, W.R., hay, C.J., Mitrovica, J.X., Morrow, E.D., Rahmstorf, S., 2016. Temperature-driven global sea-level variability in the Common Era. Proc. Natl. Acad. Sci. Unit. States Am. 113 (11), 1434–1441.
Lambeck, K., Rouby, H., Purcell, A., Sun, Y., Sambridge, M., 2014. sea level and global ice volumes from the last glacial maximum to the Holocene. Proc. Natl. Acad. Sci. Unit. States Am. 111 (43), 15296–15303.
Leclercq, P.W., Oerlemans, J., Cogley, J.G., 2011. Estimating the glacier contribution to sea-level rise for the period 1800–2005. Surv. Geophys. 32, 519–535.
Lehner, F., Born, A., Raible, C.C., Stocker, T.F., 2013. Amplified inception of European little ice age by sea ice-ocean-atmosphere feedbacks. J. Clim. 26, 7589–7602.
Long, A.J., Innes, J.B., Shennan, I., Tooley, M.J., 1999. Coastal stratigraphy: a case study from Johns River, Washington, USA. In: Jones, A.P., Tucker, M.E., Hart, J.K. (Eds.), The Description and Analysis of Quaternary Stratigraphic Field Sections. Quaternary Research Association, London. Technical Guide No. 7.
Long, A.J., Waller, M.P., Stupples, P., 2006. Driving mechanisms of coastal change: peat compaction and the destruction of late Holocene coastal wetlands. Mar. Geol. 225, 63–84.
Long, M., Boylan, N., 2013. Predictions of settlement in peat soils. Quat. J. Eng. Geol. Hydrogeol. 46, 303–322.
Manly, B.F.J., 1997. Randomization, Bootstrap and Monte Carlo Methods in Biology. Chapman and Hall, London.
Mann, M.E., Zhang, Z., Hughes, M.K., Bradley, R.S., Miller, S.K., Rutherford, S., Ni, F., 2008. Proxy-based reconstructions of hemispheric and global surface temperature variations over the past two millennia. Proc. Natl. Acad. Sci. Unit. States Am. 105 (36), 13252–13257.
Mann, M.E., Zhang, Z., Rutherford, S., Bradley, R.S., Hughes, M.K., Shindell, D., Ammann, C., Faluvegi, G., Ni, F., 2009. Global signatures and dynamical origins of the little ice age and medieval climate anomaly. Science 326, 1256–1260.
Marcott, S.A., Shakun, J.D., Clark, P.U., Mix, A.C., 2013. A reconstruction of regional and global temperature for the past 11,300 years. Science 339, 1198–1201.
Marshall, J., Johnson, H., Goodman, J., 2001. A study of the interaction of the North Atlantic Oscillation with ocean circulation. J. Clim. 14, 1399–1421.
Marshall, W., 2015. Chronohorizons: indirect and unique event dating methods for sea-level reconstructions. In: Shennan, I., Long, A.J., Horton, B.P. (Eds.), Handbook of Sea-level Research. Wiley, Chichester, pp. 372–385.
Marzeion, B., Leclercq, P.W., Cogley, J.G., Jarosch, A.H., 2015. Global reconstructions of glacier mass change during the 20th century are consistent. Cryosphere 9, 2399–2404.
Mauquoy, D., van Geel, B., 2007. Mire and peat macros. In: Elias, S.A. (Ed.), Encyclopedia of Quaternary Science. Elsevier, Oxford.
McCarthy, G.D., Haigh, I.D., Hirschi, J.J.-M., Grist, J.P., Smeed, D.A., 2015. Ocean impact on decadal Atlantic climate variability revealed by sea-level observations. Nature 521, 508–512.
McManus, J.F., Francois, R., Gherardi, J.-M., Keigwin, L.D., Brown-Leger, S., 2004. Collapse and rapid resumption of the Atlantic meridional circulation linked to deglacial climate changes. Nature 428, 834–837.
Mitovica, J.X., Forte, A.M., Simons, M., 2000. A reappraisal of postglacial decay times from Richmond Gulf and James Bay, Canada. Geophys. J. Int. 142, 783–800.
Mitrovica, J.X., Gomez, N., Clark, P.U., 2009. The sea-level fingerprint of West Antarctic collapse. Science 323, 753.
Mitrovica, J.X., Tamisiea, M.E., Davis, J.L., Milne, G.A., 2001. Recent mass balance of polar ice sheets inferred from patterns of global sea-level change. Nature 409, 1026–1029.
Mimeault, M., 2005. Gaspesie: a Brief History. Les Presses de l'Université Laval.
Moffa-Sánchez, P., Born, A., Hall, I.R., Thornalley, D.J.R., Barker, S., 2014. Solar forcing of North Atlantic surface temperature and salinity over the past millennium. Nat. Geosci. 7, 275–278.
Moreno-Chamarro, E., Zanchettin, D., Lohmann, K., Jungclaus, J.H., 2017. An abrupt weakening of the subpolar gyre as a trigger of Little Ice Age-type episodes. Clim. Dynam. 48, 727–744.
Murray, J.W., 1971. An Atlas of British Recent Foraminiferids. American Elsevier Publishing Company Inc., New York.
Murray, J.W., 1976. Comparative studies of living and dead benthic foraminiferal distributions. In: Hedley, R.H., Adams, C.G. (Eds.), Foraminifera, pp. 45–109.
Murray, J.W., 1979. British Nearshore Foraminiferids. Academic Press, London, New York and San Francisco.
Nriagu, J.O., 1990. The rise and fall of leaded gasoline. Sci. Total Environ. 92, 13–28.
Olejczyk, P., Gray, J.T., 2007. The relative influence of Laurentide and local ice sheets during the last glacial maximum in the eastern Chic-Chocs Range, northern Gaspé Peninsula, Québec. Can. J. Earth Sci. 44, 1603–1625.
Ortega, P., Lehner, F., Swingedouw, D., Masson-Delmotte, V., Raible, C.C., Casado, M., Yiou, P., 2015. A model-tested North Atlantic Oscillation reconstruction for the past millennium. Nature 523, 71–74.
Parsons, M.B., Cranston, R.E., 2005. Distribution, transport, and sources of metals in marine sediments near a coastal lead smelter in northern New Brunswick. Geol. Surv. Can. Bull. 584.
Parsons, M.B., Cranston, R.E., 2006. Influence of lead smelter emissions on the distribution of metals in marine sediments from Chaleur Bay, eastern Canada. Geochem. Explor. Environ. Anal. 6, 259–276.
Paul, M.A., Barras, B.F., 1998. A geotechnical correction for post-depositional sediment compression: examples from the Forth valley, Scotland. J. Quat. Sci. 13, 171–176.
Peltier, W.R., Argus, D.F., Drummond, R., 2015. Space geodesy constrains ice age terminal deglaciation: the global ICE_6G_C (VM5a) model. J. Geophys. Res.: Solid Earth 120, 450–487.
Plater, A.J., Kirby, J.R., Boyle, J.F., Shaw, T., Mills, H., 2015. Loss on ignition and organic content. In: Shennan, I., Long, A.J., Horton, B.P. (Eds.), Handbook of Sea-level Research. Wiley, Chichester, pp. 312–330.
Preuss, H., 1979. Progress in computer evaluation of sea-level data within the IGCP project no. 61. In: Flexor, I. (Ed.), International Symposium on Coastal Evolution in the Quaternary (Sao-Paulo, Brazil).
Pronk, A.G., Bobrowsky, P.T., Parkhill, M.A., 1989. An interpretation of Late Quaternary glacial flow indicators in the Baie des Chaleurs region, northern New Brunswick. Géogr. Phys. Quaternaire 43 (2), 179–190.
R Development Core Team, 2017. R: a Language and Environment for Statistical Computing. R Foundation of Statistical Computing, Vienna, Austria, ISBN 3-900051-070. http://www.R-project.org.
Rahmstorf, S., Box, J.E., Feulner, G., Mann, M.E., Robinson, A., Rutherford, S., Schaffernicht, E.J., 2015. Exceptional twentieth-century slowdown in Atlantic Ocean overturning circulation. Nat. Clim. Change 5, 475–479.
Rampton, V.N., Gauthier, R.C., Thibault, J., Seaman, A.A., 1984. Quaternary Geology of New Brunswick. Geological Survey of Canada. Memoir 416.
Reimer, P.J., Baillie, M.G.L., Bard, E., Bayliss, A., Beck, J.W., Blackwell, P.G., Ramsey, C.B., Buck, C.E., Burr, G.S., Edwards, R.L., Friedrich, M., Grootes, P.M., Guilderson, T.P., Hajdas, I., Heaton, T.J., Hogg, A.G., Hughen, K.A., Kaiser, K.F., Kromer, B., McCormac, F.G., Manning, S.W., Reimer, R.W., Richards, D.A., Southon, J.R., Talamo, S., Turney, C.S.M., van der Plicht, J., Weyhenmeyer, C.E., 2009. IntCal09 and Marine09 radiocarbon age calibration curves, 0-50,000 years CAL BP. Radiocarbon 51 (4), 1111–1150.
Rémillard, A.M., St-Onge, G., Bernatchez, P., Hétu, B., Buylaert, J.-P., Murray, A.S., Vigneault, B., 2016. Chronology and stratigraphy of the Magdalen Islands archipelago from the last glaciation to the early Holocene: new insights into the glacial and sea-level history of eastern Canada. Boreas 45, 604–628.
Saher, M.H., Gehrels, W.R., Barlow, N.L.M., Long, A.J., Haigh, I.D., Blaauw, M., 2015. Sea-level changes in Iceland and the influence of the North Atlantic Oscillation during the last half millennium. Quat. Sci. Rev. 108, 23–36.
Sallenger Jr., A.H., Doran, K.S., Howd, P.A., 2012. Hotspot of accelerated sea-level rise on the Atlantic coast of North American. Nat. Clim. Change 2, 884–888.
Schafer, C.T., 1977. Distribution and depositional history of sediments in Baie des Chaleurs, Gulf of St. Lawrence. Can. J. Earth Sci. 14, 593–605.
Scott, D.B., Greenberg, D.A., 1983. Relative sea-level rise and tidal development in the Fundy tidal system. Can. J. Earth Sci. 20, 1554–1564.
Scott, D.B., Medioli, F.S., 1978. Vertical zonations of marsh foraminifera as accurate indicators of former sea-levels. Nature 272, 528–531.
Scott, D.B., Medioli, F.S., 1980. Quantitative Studies of Marsh Foraminiferal Distributions in Nova Scotia: Implications for Sea Level Studies, vol. 17. Cushman Foundation for Foraminiferal Research. Special Publication No.
Scott, D.B., Medioli, F.S., Duffett, T.E., 1984. Holocene rise of Relative sea level at sable Island, Nova Scotia, Canada. Geology 12, 173–176.
Scott, D.B., Williamson, M.A., Duffett, T.E., 1981. Marsh foraminifera of Prince Edward Island: their recent distribution and application for former sea level studies. Marit. Sediments Atl. Geol. 17, 98–129.
Sévellec, F., Fedorov, A.V., Liu, W., 2017. Arctic sea-ice decline weakens the Atlantic meridional overturning circulation. Nat. Clim. Change 7, 604–610.
Shennan, I., Long, A.J., Horton, B.P., 2015. Handbook of Sea-level Research. Wiley, Chichester.
Simpson, G.L., 2007. Analogue methods in palaeoecology: using the analogue package. J. Stat. Software 22 (2), 1–29.
Slangen, A.B.A., Church, J.A., Agosta, C., Fettweis, X., Marzeion, B., Richter, K., 2016. Anthropogenic forcing dominates global mean sea-level rise since 1970. Nat. Clim. Change 6, 701–705.
Southall, K.E., Gehrels, W.R., Hayward, B.W., 2006. Foraminifera in a New Zealand salt marsh and their suitability as sea-level indicators. Mar. Micropaleontol. 60, 167–179.
St-Onge, G., Duchesne, M.J., Lajeunesse, P., 2003. Marine geology of the st. Lawrence estuary. IOP Conf. Ser. Earth Environ. Sci. 14 https://doi.org/10.1088/1755-1315/14/1/012003.
Stine, R., 1990. An introduction to bootstrap methods: examples and ideas. In: Fow, J., Long, J.S. (Eds.), Modern Methods of Data Analysis. Sage, Newbury Park, pp. 325–373.
Strachan, K.L., Hill, T.R., Finch, J.M., Barnett, R.L., 2015. Vertical zonation of foraminifera assemblages in Galpins salt marsh, South Africa. J. Foraminifer. Res. 45 (1), 29–41.
Strachan, K.L., Hill, T.R., Finch, J.M., Barnett, R.L., Frenzel, P., 2017. Distribution of salt-marsh foraminifera in two South African estuaries and the application as sea-level indicators. J. Coast Res. 33 (3), 619–631.
Stea, R.R., 2004. The Appalachian Glacier Complex in maritime Canada. In: Ehlers, J., Gibbard, P.L. (Eds.), Quaternary Glaciations - Extend and Chronology, Part II : North America. Elsevier, New York, pp. 213–232.
Stea, R.R., Seaman, A.A., Pronk, T., Parkhill, M.A., Allard, S., Utting, D., 2011. The

Appalachian Glacier Complex in maritime Canada. In: Ehlers, J., Gibbard, P.L., Hugues, P.D. (Eds.), Quaternary Glaciations - Extend and Chronology. Elsevier, New York, pp. 631–659.
Stuiver, M., Polach, H.A., 1977. Discussion reporting of ^{14}C data. Radiocarbon 19 (3), 355–363.
Stuiver, M., Reimer, P.J., 1986. A computer program for radiocarbon age calibration. Radiocarbon 28 (2B), 1022–1030.
Syvitski, J.P.M., 1992. Marine geology of Baie des Chaleurs. Géogr. Phys. Quaternaire 46 (3), 331–348.
Syvitski, J.P.M., Praeg, D.B., 1989. Quaternary sedimentation in the St. Lawrence Estuary and adjoining areas, eastern Canada: an overview based on high-resolution seismo-stratigraphy. Géogr. Phys. Quaternaire 43 (3), 291–310.
Telford, R.J., Birks, H.J.B., 2005. The secret assumption of transfer functions: problems with spatial autocorrelation in evaluating model performance. Quat. Sci. Rev. 24 (20–21), 2173–2179.
ter Braak, C.J.F., Looman, C.W.N., 1986. Weighted averaging, logistic regression and the Gaussian response model. Vegetatio 65, 3–11.
ter Braak, C.J.F., Prentice, I.C., 1988. A theory of gradient analysis. Adv. Ecol. Res. 18, 271–317.
ter Braak, Šmilauer, 2012. Canoco 5: software for multivariate data exploration, testing and summarization. Biometrics. Plant Research International, The Netherlands and Petr Šmilauer, Czech Republic.
Thomas, L.H., Grant, D.R., Grace, D.E., 1973. A late pleistocene marine shell deposit at shippegan, new Brunswick. Can. J. Earth Sci. 10, 1329–1332.
Tremblay, B., 2002. Les milieu humides côtieres du sud de la Gaspésie. Document présenté à la Société de la faune et des parcs du Québec et au ministère des Pêches et des Océans du Canada.
Troels-Smith, J., 1955. Characterization of unconsolidated sediments. In: Danmarks Geologiske Undersogelse. Series IV, vol. 3, pp. 38–73.
Trouet, V., Esper, J., Graham, N.E., Baker, A., Scourse, J.D., Frank, D.C., 2009. Persistent positive North Atlantic oscillation mode dominated the medieval climate anomaly. Science 324, 78–80.
Trouet, V., Scourse, J.D., Raible, C.C., 2012. North Atlantic storminess and Atlantic meridional overturning circulation during the last millennium: reconciling contradictory proxy records of NAO variability. Global Planet. Change 84 (85), 48–55.
Ullman, D.J., Carlson, A.E., Hostetler, S.W., Clark, P.U., Cuzzone, J., Milne, G.A., Winsor, K., Caffee, M., 2016. Final Laurentide ice-sheet deglaciation and Holocene climate sea-level change. Quat. Sci. Rev. 151, 49–59.
Vacchi, M., Engelhart, S.E., Nikitina, D., Ashe, E., Peltier, W.R., Roy, K., Kopp, R.E., Horton, B.P., 2018. Postglacial relative sea-level histories along the eastern Canadian coastline. Quat. Sci. Rev. 201 (1), 124–146.
van de Plassche, O., 1982. Sea-level change and water-level movements in The Netherlands during the Holocene. Meded. Rijks Geol. Dienst 36 (1).
van de Plassche, O., Bohncke, S.J.P., Makaske, B., van der Plicht, J., 2005. Water-level changes in the Flevo area, central Netherlands (5300-1500 BC): implications for relative mean sea-level rise in the Western Netherlands. Quat. Int. 133–134, 77–3.
Veillette, J., Cloutier, M., 1993. Géologie des formations en surface, Gaspésie, Québec [document cartographique]. Commission géologique du Canada, carte 1804A. Échelle 1, 125, 000.
Viau, A.E., Gajewski, K., 2009. Reconstructing millennial-scale, regional paleoclimates of boreal Canada during the Holocene. J. Clim. 22, 316–330.
Wanamaker, A.D., Butler, P.G., Scourse, J.D., Heinemeier, J., Eiriksson, J., Knudsen, K.L., Richardson, C.A., 2012. Surface changes in the North Atlantic meridional overturning circulation during the last millennium. Nat. Commun. 3 (899) https://doi.org/10.1038/ncomms1901 |.
Wang, J., Yang, B., Ljungqvist, F.C., Luterbacher, J., Osborn, T.J., Briffa, K.R., Zorita, E., 2017. Internal and external forcing of multidecadal Atlantic climate variability over the past 1,200 years. Nat. Geosci. 10, 512–517.
Watcham, E.P., Shennan, I., Barlow, N.L.M., 2013. Scale considerations in using diatoms as indicators of sea-level change: lessons from Alaska. J. Quat. Sci. 28 (2), 165–179.
Whitlock, C., Larsen, C., 2001. Charcoal as a fire proxy. In: Smol, J.P., Birks, H.J.B., Last, W.M. (Eds.), Tracking Environmental Change Using Lake Sediments. Volume 3: Terrestrial, Algal, and Siliceous Indicators. Kluwer Academic Publishers, Dordrecht, The Netherlands.
Williams, H., 1979. Appalachian orogen in Canada. Can. J. Earth Sci. 16 (3), 792–807.
Wood, S.N., 2018. Mixed GAM computation vehicle with automatic smoothness estimation. R package version 1.8-24. https://cran.r-project.org/package=mgcv.
Wood, S.N., 2017. Generalized Additive Models: an Introduction with R, second ed. Chapman and Hall/CRC, ISBN 9781498728331.
Woodroffe, S.A., Long, A.J., Milne, G.A., Bryant, C.L., Thomas, A.L., 2015. New constraints on late Holocene eustatic sea-level changes from Mahé, Seychelles. Quat. Sci. Rev. 115, 1–16.
Woodworth, P.L., Morales Maqueda, M.A., Gehrels, W.R., Roussenov, V.M., Williams, R.G., Hughes, C.W., 2017. Variations in the difference between mean sea level measured either side of Cape Hatteras and their relation to the North Atlantic Oscillation. Clim. Dynam. 49, 2451–2469.
Wright, A.J., Edwards, R.J., van de Plassche, O., 2011. Reassessing transfer-function performance in sea-level reconstruction on benthic salt-marsh foraminifera from the Atlantic coast of NE North America. Mar. Micropaleontol. 81, 43–62.
Wright, A.J., van de Plassche, O., 2001. Field Guide to the Quaternary West Coast of Newfoundland. Geological Association of Canada - Mineralogical Association of Canada.
Yang, Q., Dixon, T.H., Myers, P.G., Bonin, J., Chambers, D., van den Broeke, M.R., Ribergaard, M.H., Mortensen, J., 2016. Recent increases in Arctic freshwater flux affects Labrador Sea convection and Atlantic overturning circulation. Nat. Commun. 7, 10525.
Zemp, M., Frey, H., Gärtner-Roer, I., Nussbaumer, S.U., Hoelzle, M., Paul, F., Haeberli, W., Denzinger, F., Ahlstrøm, A.P., Anderson, B., Bajracharya, S., Baroni, C., Braun, L.N., Caceres, B.E., Casassa, G., Cobos, G., Davila, L.R., Delgado Grandos, H., Demuth, M.N., Espizua, L., Fischer, A., Fujita, K., Gadek, B., Ghazanfar, A., Hagen, J.O., Holmlund, P., Karimi, N., Li, Z., Pelto, M., Pitte, P., Popovnin, V.V., Portocarrero, C.A., Prinz, R., Sangewar, C.V., Severskiy, I., Sigurdsson, O., Soruco, A., Usubaliev, R., Vincent, C., 2015. Historically unprecedented global glacier decline in the early 21st century. J. Glaciol. 61 (228), 745–761.